
Article:
Vu, T.-V., Nguyen-Van, H., Nguyen, C.H. et al. (2 more authors) (2021) Meshfree analysis of functionally graded plates with a novel four-unknown arctangent exponential shear deformation theory. Mechanics Based Design of Structures and Machines, 51 (2). pp. 1082-1114. ISSN 1539-7734

https://doi.org/10.1080/15397734.2020.1863227

Meshfree analysis of functionally graded plates with a novel four-unknown arctangent exponential shear deformation theory

T-V. Vu, H. Nguyen-Van, C.H. Nguyen, T-P. Nguyen, J.L. Curiel-Sosa

MECHANICS BASED DESIGN OF STRUCTURES AND MACHINES
https://doi.org/10.1080/15397734.2020.1863227

ABSTRACT

A novel refined arctangent exponential shear deformation theory (RAESDT) is presented for analysis the mechanical behavior of both isotropic and sandwich FGM plates. Material properties are set to be isotropic at each point and varied across the thickness direction obeying to a power-law distribution of the volume fraction gradation with respect to FGM core or skins of the plate. Unlike high-order shear deformation plate theories based on five or more variables, the displacement field of the novel RAESDT using arctangent exponential variations in planed displacements were approximated by only four unknowns, satisfying naturally tangential stress-free conditions at the plate surfaces and leading to reduce computational efforts. In accordance with RAESDT and enhanced moving kriging interpolation (EMKI)-based meshfree method with a new quadrature correlation function is introduced for the numerical modeling. Numerical validations with different plate configurations, geometries, length to thickness ratios and boundaries conditions are conducted. The obtained results are compared with the corresponding solutions available in the literature showing the accuracy and efficiency of the present approach.

1. Introduction

Functionally graded (FG) materials (FGMs) are advanced composite materials in which the composition smoothly changes over the thickness direction by mixing two different materials. Nowadays, FGMs are being employed in many engineering fields due to their prominent features such as smooth distribution of leftover stresses, enhanced thermal conductivity, high fracture toughness, low residual and thermal stresses and an increase in strength-to-weight ratio when compared to the other engineering materials. A wide range of applications of FGMs in various industries forced researchers developing accurate analytical and numerical techniques for analysis the mechanical behaviors of the FG plate.

In general, plate deformation theories can be classified into two types: displacement-based and stress-based theories. Normally, the plate displacement-based theories can be divided into two

categories: the classical plate theory (CPT) (Love 1888; Kirchhoff 1850), and shear deformation plate theories involved the first-order shear deformation theory (FSDT) (Reissner 1945; Mindlin 1951), high-order shear deformation theory (HSDT) and refined plate theory (RPT) (Senthilnathan et al. 1987). It is well known that the CPT and FSDT are not suitable for the analysis of thick plates, since the former does not consider shear effect, while the latter assumes that the shear stress is a constant through the plate thickness. To overcome this limitation, the HSDT is developed to simulate the distribution of transverse shear stresses across the plate thickness by using either polynomial functions (e.g., the third-order shear deformation theory (TSDT) of Reddy 1984 and of Shi 2007) or non-polynomial functions (e.g., the sinusoidal theory of Touratier 1991; hyperbolic theory of Soldatos 1992; exponential theory of Karama, Afaq, and Mistou 2003). The HSDT has a widely apply to analysis mechanical behavior of the difference plate structures (Lim 2016; Cheshmeh et al. 2020; Dastjerdi, Rashahmadi, and Meguid 2020; Garg, Chalak, and Chakrabarti 2020; Hachemi and Cherif 2020), but compared to the RPT, it is computationally expensive. The RPT based on the assumption of the transverse displacement is composed of the bending and shear components, and only the bending component of the transverse deflection causes the rotations in the TSDT. Moreover, it conserves the advantages of TSDT but reduces one unknown variable compared to the TSDT, that is important for enhancing the computational efficiency. The works of some researchers (Vu, Curiel-Sosa, and Bui 2018b; Farzad, Nouraei, and Dabbagh 2020) are interesting examples in this context. Recently, Rahmani et al. (2020) and Menasria, Kaci, and Bousahla (2020) develop a new simple higher-order shear deformation theory (SHSDT) with the four-variable unknown as the same as the CPT and RPT for analyses of the bending and free vibration of FG-sandwich plates, but its displacement field included the undetermined integral components that could be resolved by the Navier-type method. The advantage of SHSDT compared to that of RPT is the reduction of numerical computational time and alleviating engineering analysis for the plate structures solved by the analytical methods.

On the other hand, some researchers have also studied the mechanical behaviors of FGM plates wherein the material gradient in the in-plane direction of the plate (Liu, Wang, and Chen 2010; Chu et al. 2016; Lieu et al. 2018). Recently, Amirpour et al. (2018, 2019) conduct the numerical and experimental study for the free vibration and static bending of the simply supported 3D printed polymeric FG with a variation of material stiffness and density along their length based on the HSDT and 3D-digital image correlation approach.

It is widely known that one of the main advantages of RPT is that it possesses naturally free from shear locking for thin plate case and has fewer variables than HSDT. However, RPT requires C^1 continuity hindering the natural use from C^0 finite element method (FEM). One of the ways to overcome this drawback is to employ meshfree or meshless methods.

A detail review of the recent meshfree methods for laminated and functionally graded plates and shells was presented by Liew, Zhao, and Ferreira (2011). According to the formulation procedure, they are classified into three categories: meshless weak form methods, meshless strong form methods, meshless weak–strong form methods. Among the well-known methods based on the weak forms, meshless method by using the moving kriging (MK) interpolation (MKI) possesses a notable feature is that its shape function inherited the Kronecker delta property. Consequently, essential boundary conditions are imposed as straightforward as for the FEM without any special techniques. Unfortunately, the quality of traditional MKI shape function affected heavily from correlation parameter leading to instable solutions. Recently, Thai, Vuong, and Nguyen-Xuan (2016) try to overcome this shortcoming by using a complicated quartic polynomial form for the correlation function to construct the MKI shape function.

In our work, for the first time, the formulation of refined arctangent exponential shear deformation theory (RAESDT) in accordance with meliorated moving kriging interpolation-based (EMKI) meshfree method with a new quadrature correlation function for mechanical behavior

analysis of the FG plates. The novelty of this study is to propose a distributed function toward a better representation of the transverse shear stress in the plate thickness and gives the mechanical behavior of the FG plates as much close as possible to the three-dimensional elasticity approach. The proposed correlation function is used to eliminate using correlation parameters of its conventional form gaining accurate solutions. Several problems of static bending, free vibration and compressive buckling of FG plates with different configurations, shape geometries, length to thickness ratios or boundary conditions are then computed by the proposed approach. The numerical validations are conducted to demonstrate the accuracy, stability and effectiveness of the present method.

2. Theoretical formulations

2.1. FG plate types

Consider a typical rectangular plate with the total thickness h, the width a and the length b, referred to the Cartesian coordinates (x, y, z) as shown in Figure 1a. The top and bottom plate faces locate at $z = \pm h/2$, and plate edges are parallel to axes x and y. The plate material properties depend on all material properties and volume fractions from its constituent materials. In this study, three different types of FG plates are considered: isotropic FG plates, sandwich plates with FG core and homogeneous skins and sandwich plates with FG skins and homogeneous core. Both of them have no interfaces between core and skins.

2.1.1. Isotropic FG plates (IF)

An IF plate possesses material inhomogeneous assumed to be isotropic with a volume fraction changing smoothly such that plate bottom and top skin are pure metal and ceramic, respectively. Its effective material properties $P_e(z)$ such as the Young's modulus $E(z)$, mass density $\rho(z)$, or Poisson's ratio $\nu(z)$ is defined according to the power-law distribution (Reddy 2000) as follows:

$$P_e(z) = P_c V_c(z) + P_m V_m(z), \quad V_c(z) = \left(\frac{1}{2} + \frac{z}{h}\right)^{\eta}, \quad V_m(z) = 1 - V_c(z), \quad -\frac{h}{2} \le z \le \frac{h}{2} \tag{1a, 1b, 1c, 1d}$$

wherein subscripts m, c are defined to the metal, ceramic constituents, respectively; η is the gradient index; P_c and P_m are denoted to the ceramic and metal constituent materials, respectively. Figure 1b shows a ceramic volume fraction $V_c(z)$ distribution against the coordinate z/h by varying the gradient index η.

2.1.2. Sandwich plate with FG core and homogeneous skins (FCHS)

A sandwich FCHS plate consists of three layers (see Figure 2a). Its core material is made of FGMs with effective properties varying smoothly by the power-law rule in the z direction.

Its two material skins are homogeneous material wherein skin top and bottom are respectively fully-metallic and ceramic. Volume ceramic fraction of the FCHS plate given by Eq. (2) as follows:

$$\begin{aligned} V_c^1(z) &= 0, && -\frac{h}{2} = z_1 \le z \le z_2 \\ V_c^2(z) &= \left(\frac{z - z_2}{z_3 - z_2}\right)^{\eta}, && z_2 \le z \le z_3 \\ V_c^3(z) &= 1, && z_3 \le z \le z_4 = \frac{h}{2} \end{aligned} \tag{2a, 2b, 2c}$$

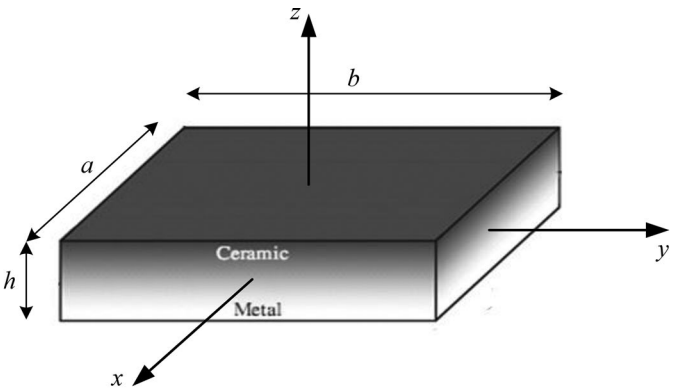

(a)

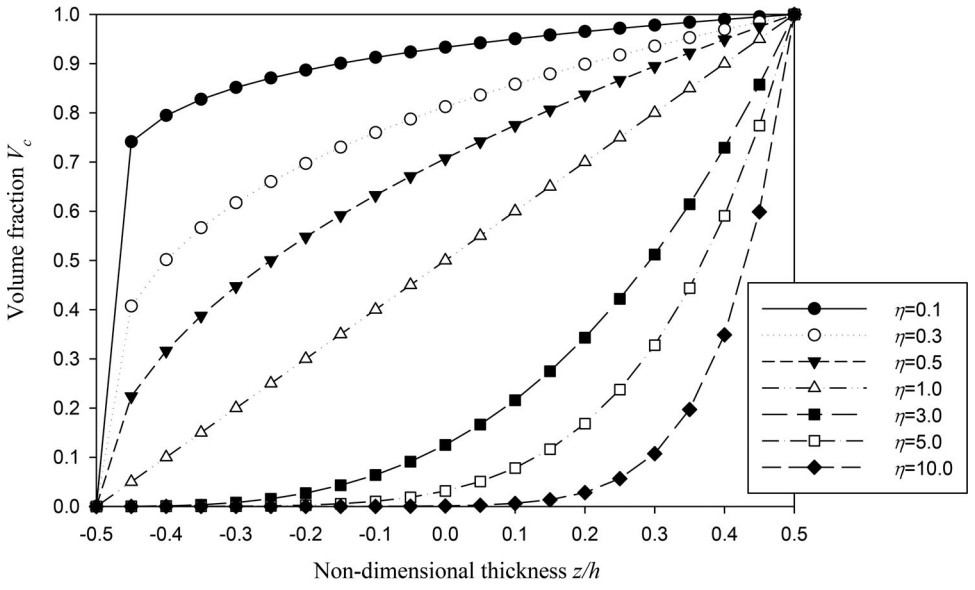

(b)

Figure 1. Isotropic FG rectangular plate: (a) Geometric shape and Cartesian coordinates (b) Variations of $V_c(z)$ for h/R under various gradient indices η.

where $V_c^i (i = 1, 2, 3)$ represents the volume ceramic fraction of layer i, and the core thickness is determines by $(z_3 - z_2)$.

2.1.3. Sandwich plates with homogeneous core and FG skins (HCFS)

A sandwich HCFS plate is also made of three layers. Two plate FG skins are composed from a mixture of metal and ceramic based on the power-law rule, while the plate core is pure ceramic (see Figure 2b). Assuming that levels $z = -h/2,\ z = h/2$ are metal-rich, and levels $z = z_2,\ z = z_3$ are ceramic-rich, the volume ceramic fraction for each layer can be expressed as

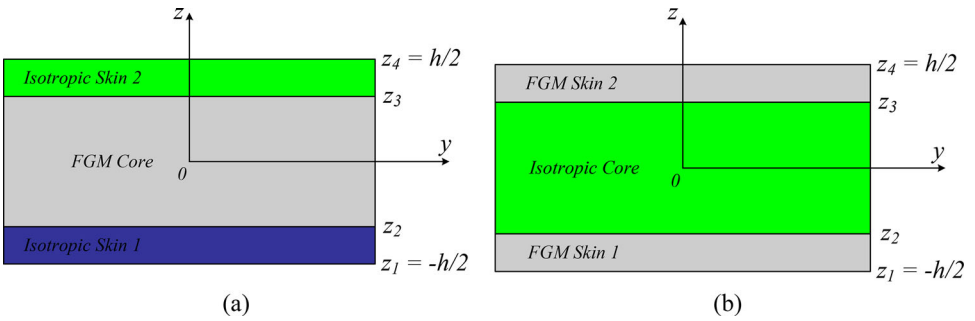

Figure 2. Schematic diagram of sandwich FG plates: (a) FCHS type; (b) HCFS type.

$$V_c^1(z) = \left(\frac{z - z_1}{z_2 - z_1}\right)^{\eta}, \quad -h/2 = z_1 \le z \le z_2$$
$$V_c^2(z) = 1, \qquad z_2 \le z \le z_3 \tag{3a, 3b, 3c}$$
$$V_c^3(z) = \left(\frac{z_4 - z}{z_4 - z_3}\right)^{\eta}, \quad z_3 \le z \le z_4 = h/2$$

wherein thickness of the top and bottom skins are $(z_4 - z_3)$ and $(z_2 - z_1)$, respectively. The thickness of each layer may be varied. For the brevity, the thickness ratio of each layer from bottom to top is defined by the combination of three numbers, i.e. $(1/1/1)$, $(2/2/1)$, and so on.

2.2. Refined arctangent shear deformation theory

Consider a domain $\wp$ in space $\Re^2$ located at the middle plane of the FG plate. Based on assumptions of the refined plate theory (Senthilnathan et al. 1987), the displacement field of the refined arctangent exponential shear deformation theory (RAESDT) is assumed to be

$$u(x,y,z,t) = u_0(x,y,t) - z\frac{\partial w_b(x,y,t)}{\partial x} + g(z)\frac{\partial w_s(x,y,t)}{\partial x}$$
$$v(x,y,z,t) = v_0(x,y,t) - z\frac{\partial w_b(x,y,t)}{\partial y} + g(z)\frac{\partial w_s(x,y,t)}{\partial y} \tag{4a, 4b, 4c}$$
$$w(x,y,z,t) = w_b(x,y,t) + w_s(x,y,t)$$

where u_0 and v_0 are in-plane displacements of a point on the plate middle plane; u, v and w are components of displacement vector along the $x-, y-$ and $z-$axis, respectively; w_b and w_s are bending and shear components of the transverse deflection; g is a shape function given by $g(z) = f(z) - z$ with $f(z) = \tan^{-1}(ze^{-2(z/h)^2})$ represents the effective shape function of transverse shear strains and stresses along the thickness. It is equal to zero at $z = \pm h/2$ satisfying the condition of shear stress τ_{xz} and τ_{yz} at the free surfaces. Using the assumption of the infinitesimally small of Lagrangian strains, the strain and displacement relationship can be described by:

$$\begin{Bmatrix} \varepsilon_x \\ \varepsilon_y \\ \gamma_{xy} \\ \gamma_{xz} \\ \gamma_{yz} \end{Bmatrix} = \begin{Bmatrix} \partial u_0/\partial x - z\partial^2 w_b/\partial x^2 + g\partial^2 w_s/\partial x^2 \\ \partial v_0/\partial y - z\partial^2 w_b/\partial y^2 + g\partial^2 w_s/\partial y^2 \\ \partial u_0/\partial y + \partial v_0/\partial x - 2z\partial^2 w_b/\partial x\partial y + 2g\partial^2 w_s/\partial x\partial y \\ f'\partial w_s/\partial x \\ f'\partial w_s/\partial y \end{Bmatrix} \tag{5a, 5b, 5c, 5d, 5e}$$

or expressed in a shortened form:

$$\boldsymbol{\varepsilon} = \begin{Bmatrix} \boldsymbol{\varepsilon}_0 \\ 0 \end{Bmatrix} + \begin{Bmatrix} z\boldsymbol{\kappa}^b + g\boldsymbol{\kappa}^s \\ f'\boldsymbol{\gamma} \end{Bmatrix} \tag{6a, 6b}$$

with

$$\boldsymbol{\varepsilon}_0 = \left\{ \partial u_0/\partial x \quad \partial v_0/\partial y \quad \partial u_0/\partial y + \partial v_0/\partial x \right\}^T, \quad \boldsymbol{\kappa}^b = \left\{ -\frac{\partial^2 w_b}{\partial x^2} \quad -\frac{\partial^2 w_b}{\partial y^2} \quad -2\frac{\partial^2 w_b}{\partial x \partial y} \right\}^T$$
$$\boldsymbol{\kappa}^s = \left\{ \partial^2 w_s/\partial x^2 \quad \partial^2 w_s/\partial y^2 \quad 2\partial^2 w_s/\partial x \partial y \right\}^T, \quad \boldsymbol{\gamma} = \left\{ \partial w_s/\partial x \quad \partial w_s/\partial y \right\}^T \tag{7a, 7b, 7c, 7d}$$

3. EMKI-based meshless method for analyzing the FG plate

3.1. Meliorated moving kriging shape function

According to the traditional MKI method (Bui, Nguyen, and Nguyen 2009), a function $\tilde{\mathbf{u}}^h(\overline{\mathbf{x}})$ can be approximated by using a known discrete function $\hat{\mathbf{u}}(\hat{\mathbf{x}})$ consisted of different nodal points $\hat{x}_i (i \in [1, n_r])$ within a subdomain $\wp_x \subseteq \wp$, and written by:

$$\tilde{\mathbf{u}}^h(\overline{\mathbf{x}}) = \left[\hat{\mathbf{p}}^T(\hat{\mathbf{x}})\hat{\mathbf{A}} + \hat{\mathbf{r}}^T(\hat{\mathbf{x}})\hat{\mathbf{B}}\right]\hat{\mathbf{u}}(\hat{\mathbf{x}}) \text{ or in short formality } \tilde{\mathbf{u}}^h = \sum_{I=1}^{n_r} \hbar_I \hat{\mathbf{u}}_I \tag{8a, 8b}$$

wherein $\hbar_I$ is MK shape function possessed the delta function property and can be expressed as:

$$\hbar_I = \sum_{j=1}^{m_p} \hat{p}_j(\hat{\mathbf{x}})\hat{A}_{jI} + \sum_{k=1}^{n_r} \hat{r}_k(\hat{\mathbf{x}})\hat{B}_{kI} \tag{9}$$

and matrices $\hat{\mathbf{A}}$ and $\hat{\mathbf{B}}$ can be derived by

$$\hat{\mathbf{A}} = \left(\hat{\mathbf{P}}^T\hat{\mathbf{R}}^{-1}\hat{\mathbf{P}}\right)^{-1}\hat{\mathbf{P}}^T\hat{\mathbf{R}}^{-1}, \quad \hat{\mathbf{B}} = \hat{\mathbf{R}}^{-1}(\hat{\mathbf{I}} - \hat{\mathbf{P}}\hat{\mathbf{A}}) \tag{10a, 10b}$$

where $\hat{\mathbf{I}}$ denotes identity matrix, while $\hat{\mathbf{p}}(\hat{\mathbf{x}})$ in Eq. (8) can be determined by using m_p basis polynomials as follow

$$\hat{\mathbf{p}}^T(\hat{\mathbf{x}}) = \left[\hat{p}_1(\hat{\mathbf{x}}), \hat{p}_2(\hat{\mathbf{x}}), \hat{p}_3(\hat{\mathbf{x}}), ..., \hat{p}_{m_p}(\hat{\mathbf{x}})\right] \tag{11}$$

In Eq. (10), matrix $\hat{\mathbf{P}}_{n_r \times m_p}$ comprises values of the basis polynomials at n_r points in $\wp_x$ as follows

$$\hat{\mathbf{P}} = \begin{bmatrix} \hat{p}_1(\hat{x}_1) & \hat{p}_2(\hat{x}_1) & \cdots & \hat{p}_{m_p}(\hat{x}_1) \\ \hat{p}_1(\hat{x}_2) & \hat{p}_2(\hat{x}_2) & \cdots & \hat{p}_{m_p}(\hat{x}_2) \\ \vdots & \vdots & \ddots & \vdots \\ \hat{p}_1(\hat{x}_{n_r}) & \hat{p}_2(\hat{x}_{n_r}) & \cdots & \hat{p}_{m_p}(\hat{x}_{n_r}) \end{bmatrix} \tag{12}$$

In Eq. (9), vector $\hat{\mathbf{r}}(\hat{\mathbf{x}})$ is defined as follows:

$$\hat{\mathbf{r}}^T(\hat{\mathbf{x}}) = \left[\hat{R}(\hat{x}_1, \hat{\mathbf{x}}), \hat{R}(\hat{x}_2, \hat{\mathbf{x}}), ..., \hat{R}(\hat{x}_{n_r}, \hat{\mathbf{x}})\right] \tag{13}$$

wherein $\hat{R}(\hat{x}_i, \hat{x}_j)$ represents a correlation function between each arbitrary pair of the nodes located at $\hat{x}_i$ and $\hat{x}_j$. Normally, Gaussian function widely used in the traditional MKI method (Bui, Nguyen, and Nguyen 2009) and expressed by the following equations:

$$\hat{R}(\hat{x}_i, \hat{x}_j) = e^{-\theta \overline{r}_{ij}^2} \tag{14}$$

where $\overline{r}_{ij} = \|\hat{x}_i - \hat{x}_j\|$, and $\theta > 0$ is a correlation parameter dependent coordinates in support domain. It is worth noting that the quality of MK shape functions depends heavily on the correlation parameter θ caused the instability in the numerical analysis (Bui, Nguyen, and Nguyen 2009). To surmount this obstacle, we propose a new quadrature function in depending on the correlation parameter, only depending on the distance between any pairs of the nodes within $\wp_x$ given by Eq. (15):

$$\hat{R}(\hat{x}_i, \hat{x}_j) = 1 - \sqrt{2} \times \frac{\overline{r}_{ij}}{l_c} + \frac{\overline{r}_{ij}^2}{2l_c^2} \tag{15}$$

wherein l_c denotes the arithmetic mean distance between nodes. The correlation matrix $\mathbf{R}\left[\hat{R}(\hat{x}_i, \hat{x}_j)\right]_{n_r \times n_r}$ is expressed as:

$$\mathbf{R}\left[\hat{R}(\hat{x}_i, \hat{x}_j)\right] = \begin{bmatrix} 1 & \hat{R}(\hat{x}_1, \hat{x}_2) & \cdots & \hat{R}(\hat{x}_1, \hat{x}_{n_r}) \\ \hat{R}(\hat{x}_2, \hat{x}_1) & 1 & \cdots & \hat{R}(\hat{x}_2, \hat{x}_{n_r}) \\ \vdots & \vdots & \ddots & \vdots \\ \hat{R}(\hat{x}_{n_r}, \hat{x}_1) & \hat{R}(\hat{x}_{n_r}, \hat{x}_2) & \cdots & 1 \end{bmatrix} \tag{16}$$

The first derivatives and second derivatives of the MMK shape function can be illustrated as follows:

$$\hbar_{I.i} = \sum_{j=1}^{m_p} \hat{p}_{j,i}(\hat{\mathbf{x}}) \hat{A}_{jI} + \sum_{k=1}^{n_r} \hat{r}_{k,i}(\hat{\mathbf{x}}) \hat{B}_{kI}$$
$$\hbar_{I,ii} = \sum_{j=1}^{m_p} \hat{p}_{j,ii}(\hat{\mathbf{x}}) \hat{A}_{jI} + \sum_{k=1}^{n_r} \hat{r}_{k,ii}(\hat{\mathbf{x}}) \hat{B}_{kI} \tag{17a, 17b}$$

In traditional meshless methods, the rectangular or circle support can be used to gather scattered nodes for constructing the shape function. Normally, the size of the support domain determined by a circular region determined by the point of interest and a radius calculated by:

$$d_m = \alpha d_c \tag{18}$$

wherein d_c is denoted as the distance between adjacent nodes, which are the vicinity of the interest point, and α denotes a scale factor controlling the support domain size. The scale factor should be selected so that the size of influence domain comprised a certain number of nodes in order to create the MK shape function. The accuracy of the method deeply relies on the node number in the support domain; hence, an optimal value scale factor can be chosen by referring to the numerical investigations.

3.2. Emki-based meshless discretization of the FG plates

Based on the RAESDT, the field variables can be expressed in terms of the MKI meshless method as follows:

$$\tilde{\mathbf{u}}^h = \begin{bmatrix} \tilde{u}_h & \tilde{v}_h & \tilde{w}_{hb} & \tilde{w}_{hs} \end{bmatrix}^T \text{ and } \hat{\mathbf{u}}_I = \begin{bmatrix} \hat{u}_I & \hat{v}_I & \hat{w}_{bI} & \hat{w}_{sI} \end{bmatrix}^T \tag{19a,19b}$$

Substituting Eqs. (8) into (7) and then using some mathematical manipulations, one gets Eq. (20) which shows the relationship between strain and displacement of the FG plate.

$$\boldsymbol{\varepsilon}_0 = \sum_{I=1}^{n_r} \overline{\mathbf{B}}_I^m \hat{\mathbf{u}}_I,\ \ \boldsymbol{\kappa}^b = \sum_{I=1}^{n_r} \overline{\mathbf{B}}_I^{b1} \hat{\mathbf{u}}_I,\ \ \boldsymbol{\kappa}^s = \sum_{I=1}^{n_r} \overline{\mathbf{B}}_I^{b2} \hat{\mathbf{u}}_I,\ \ \boldsymbol{\gamma} = \sum_{I=1}^{n_r} \overline{\mathbf{B}}_I^s \hat{\mathbf{u}}_I \tag{20a, 20b, 20c, 20d}$$

in which

$$\overline{\mathbf{B}}_I^m = \begin{bmatrix} \hbar_{I,x} & 0 & 0 & 0 \\ 0 & \hbar_{I,y} & 0 & 0 \\ \hbar_{I,y} & \hbar_{I,x} & 0 & 0 \end{bmatrix},\ \overline{\mathbf{B}}_I^{b1} = \begin{bmatrix} 0 & 0 & -\hbar_{I,xx} & 0 \\ 0 & 0 & -\hbar_{I,yy} & 0 \\ 0 & 0 & -2\hbar_{I,xy} & 0 \end{bmatrix}$$
$$\overline{\mathbf{B}}_I^{b2} = \begin{bmatrix} 0 & 0 & 0 & \hbar_{I,xx} \\ 0 & 0 & 0 & \hbar_{I,yy} \\ 0 & 0 & 0 & 2\hbar_{I,xy} \end{bmatrix},\quad \overline{\mathbf{B}}_I^s = \begin{bmatrix} 0 & 0 & 0 & \hbar_{I,x} \\ 0 & 0 & 0 & \hbar_{I,y} \end{bmatrix} \tag{21a, 21b, 21c, 21d}$$

Static bending analysis of the FG plate under the action of a distributed force q_0 per unit area can be shown in the weak form as follows:

$$\int_{\wp} \delta\boldsymbol{\varepsilon}^T \overline{\mathbf{D}}^e \boldsymbol{\varepsilon} d\wp + \int_{\wp} \delta\boldsymbol{\gamma}^T \overline{\mathbf{D}}^s \boldsymbol{\gamma} d\wp = \int_{\Omega} \delta(\tilde{w}_{hb} + \tilde{w}_{hs}) q_0 d\wp \tag{22}$$

where

$$\boldsymbol{\varepsilon} = \begin{Bmatrix} \boldsymbol{\varepsilon}_0 \\ \boldsymbol{\kappa}^b \\ \boldsymbol{\kappa}^s \end{Bmatrix},\ \overline{\mathbf{D}}^e = \begin{bmatrix} \tilde{\mathbf{A}} & \tilde{\mathbf{B}} & \tilde{\mathbf{E}} \\ \tilde{\mathbf{B}} & \tilde{\mathbf{C}} & \tilde{\mathbf{K}}^{\varepsilon} \\ \tilde{\mathbf{E}} & \tilde{\mathbf{K}}^{\varepsilon} & \tilde{\mathbf{H}} \end{bmatrix},\ \overline{\mathbf{D}}^s = \int_{-h/2}^{h/2} \tilde{\mathbf{D}}_s dz \tag{23a, 23b, 23c}$$

the sub-matrices $\mathbf{A}, \mathbf{B}, \mathbf{C}, \mathbf{E}, \mathbf{K}^{\varepsilon}, \mathbf{H}$ and matrix $\tilde{\mathbf{D}}^s$ are given in Appendix A

Natural vibration analysis of the FG plate in the weak form can be written by:

$$\int_{\wp} \delta\boldsymbol{\varepsilon}^T \overline{\mathbf{D}}^e \boldsymbol{\varepsilon} d\wp + \int_{\wp} \delta\boldsymbol{\gamma}^T \overline{\mathbf{D}}^s \boldsymbol{\gamma} d\wp = \int_{\wp} \delta\hat{\mathbf{u}}^T \mathbf{m} \ddot{\hat{\mathbf{u}}} d\wp \tag{24}$$

the coefficients of the mass matrix $\mathbf{m}$ are given in Appendix B. The displacement fields $\tilde{\mathbf{u}}_0, \tilde{\mathbf{u}}_b, \tilde{\mathbf{u}}_s$ can be expressed as:

$$\tilde{\mathbf{u}} = \begin{Bmatrix} \tilde{\mathbf{u}}_0 \\ \tilde{\mathbf{u}}_b \\ \tilde{\mathbf{u}}_s \end{Bmatrix},\ \tilde{\mathbf{u}}_0 = \begin{Bmatrix} \hat{u}_h \\ \hat{v}_h \\ \hat{w}_{hb} + \hat{w}_{hs} \end{Bmatrix} = \sum_{I=1}^{n_r} \mathbf{N}_I^1 \hat{\mathbf{u}}_I$$
$$\tilde{\mathbf{u}}_b = \begin{Bmatrix} -\partial\hat{w}_{hb}/\partial x \\ -\partial\hat{w}_{hb}/\partial y \\ 0 \end{Bmatrix} = \sum_{I=1}^{n_r} \mathbf{N}_I^2 \hat{\mathbf{u}}_I,\ \ \tilde{\mathbf{u}}_s = \begin{Bmatrix} \partial\hat{w}_{hs}/\partial x \\ \partial\hat{w}_{hs}/\partial y \\ 0 \end{Bmatrix} = \sum_{I=1}^{n_r} \mathbf{N}_I^3 \hat{\mathbf{u}}_I \tag{25a, 25b, 25c, 25d}$$

and

$$\mathbf{N}_I^1 = \begin{bmatrix} \hbar_I & 0 & 0 & 0 \\ 0 & \hbar_I & 0 & 0 \\ 0 & 0 & \hbar_I & \hbar_I \end{bmatrix},\ \mathbf{N}_I^2 = \begin{bmatrix} 0 & 0 & -\hbar_{I,x} & 0 \\ 0 & 0 & -\hbar_{I,y} & 0 \\ 0 & 0 & 0 & 0 \end{bmatrix},\ \mathbf{N}_I^3 = \begin{bmatrix} 0 & 0 & 0 & \hbar_{I,x} \\ 0 & 0 & 0 & \hbar_{I,y} \\ 0 & 0 & 0 & 0 \end{bmatrix} \tag{26a, 26b, 26c}$$

Finally, the compressive buckling of the FG plate can be stated in the weak form as follows:

$$\int_{\wp} \delta\boldsymbol{\varepsilon}^T \overline{\mathbf{D}}^e \boldsymbol{\varepsilon} d\wp + \int_{\wp} \delta\boldsymbol{\gamma}^T \overline{\mathbf{D}}^s \boldsymbol{\gamma} d\wp + \int_{\wp} \nabla^T \delta(\tilde{w}_{hb} + \tilde{w}_{hs}) \hat{\sigma}_0 \nabla(\tilde{w}_{hb} + \tilde{w}_{hs}) d\wp = 0 \tag{27}$$

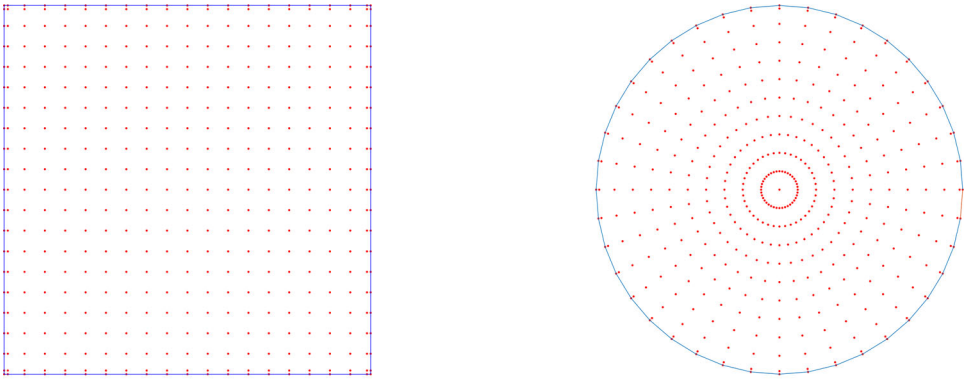

(a) (b)

Figure 3. Node redistribution to enforce clamped boundary condition: (a) Square plate, (b) circle plate.

where $\nabla^T = (\partial/\partial x \quad \partial/\partial y)$ and $\hat{\boldsymbol{\sigma}}_0 = \begin{bmatrix} \sigma_x^0 & \tau_{xy}^0 \\ \tau_{xy}^0 & \sigma_y^0 \end{bmatrix}$ denotes the initial stress matrix due to in-plane compressive forces. Substituting Eq. (19) into Eqs. (22) (24) and (27), one can obtain canonical formulations of the static bending, natural vibration and bucking problems, respectively, as follows:

$$\hat{\mathbf{K}}\hat{\mathbf{u}} = \hat{\mathbf{F}}, \quad (\hat{\mathbf{K}} - \boldsymbol{\omega}^2\hat{\mathbf{M}})\hat{\mathbf{u}} = 0, \quad \left(\hat{\mathbf{K}} - \boldsymbol{\lambda}_{\mathbf{cr}}\hat{\mathbf{K}}_{\mathbf{g}}\right)\hat{\mathbf{u}} = 0 \tag{28a, 28b, 28c}$$

wherein the stiffness matrix $\hat{\mathbf{K}}$ is given by:

$$\hat{\mathbf{K}} = \int_{\wp} \begin{Bmatrix} \overline{\mathbf{B}}_I^m \\ \overline{\mathbf{B}}_I^{b1} \\ \overline{\mathbf{B}}_I^{b2} \end{Bmatrix}^T \begin{bmatrix} \tilde{\mathbf{A}} & \tilde{\mathbf{B}} & \tilde{\mathbf{E}} \\ \tilde{\mathbf{B}} & \tilde{\mathbf{C}} & \tilde{\mathbf{K}}^{\varepsilon} \\ \tilde{\mathbf{E}} & \tilde{\mathbf{K}}^{\varepsilon} & \tilde{\mathbf{H}} \end{bmatrix} \begin{Bmatrix} \overline{\mathbf{B}}_I^m \\ \overline{\mathbf{B}}_I^{b1} \\ \overline{\mathbf{B}}_I^{b2} \end{Bmatrix} d\wp + \int_{\Omega} (\overline{\mathbf{B}}^s)^T \overline{\mathbf{D}}^s \overline{\mathbf{B}}^s d\wp \tag{29}$$

the force vector $\hat{\mathbf{F}}$ can be calculated by:

$$\hat{\mathbf{F}} = \int_{\wp} q_0 \mathbf{N} d\wp \text{ where } \mathbf{N}_I = \begin{bmatrix} 0 & 0 & \hbar_I & \hbar_I \end{bmatrix}^T \tag{30}$$

and the mass matrix $\hat{\mathbf{M}}$ has the following appearance:

$$\hat{\mathbf{M}} = \int_{\wp} \begin{Bmatrix} \mathbf{N}^1 \\ \mathbf{N}^2 \\ \mathbf{N}^3 \end{Bmatrix}^T \begin{bmatrix} \tilde{I}_0 & \tilde{I}_1 & \tilde{I}_3 \\ \tilde{I}_1 & \tilde{I}_2 & \tilde{I}_4 \\ \tilde{I}_3 & \tilde{I}_4 & \tilde{I}_5 \end{bmatrix} \begin{Bmatrix} \mathbf{N}^1 \\ \mathbf{N}^2 \\ \mathbf{N}^3 \end{Bmatrix} d\wp \tag{31}$$

the geometric stiffness matrix $\mathbf{K}_g$ can be presented by:

$$\hat{\mathbf{K}}_g = \int_{\wp} (\overline{\mathbf{B}}^g)^T \hat{\sigma}_0 \overline{\mathbf{B}}^g d\wp \text{ where } \overline{\mathbf{B}}_I^g = \begin{bmatrix} 0 & 0 & \hbar_{I,x} & \hbar_{I,x} \\ 0 & 0 & \hbar_{I,y} & \hbar_{I,y} \end{bmatrix} \tag{32a, 32b}$$

It is worth noting that matrices $\overline{\mathbf{B}}_I^{b1}$ and $\overline{\mathbf{B}}_I^{b2}$ are comprised of second order derivatives of the approximated displacement field, so the MK shape function have to C^1-continuity. Hence, the basis polynomials given by Eq. (11) having the second order polynomials in two-variable forms as follows:

Table 1. Normalized displacement $\overline{w}_c(10^{-3})$ of the Kirchhoff's homogeneous plate using different meshes and scaling factors.

		Scaling factor α							
Function	Mesh	2.0	2.10	2.20	2.30	2.40	2.50	3.00	3.50
Quadric	5×5	0.7216	0.9846	1.1195	1.1251	1.9784	2.6035	2.0607	1.9887
correlation	7×7	1.0218	1.0287	1.0373	2.4398	2.4611	2.5214	2.1597	2.1350
	9×9	1.0669	1.0705	1.3708	2.3667	2.3844	2.3103	2.2248	2.1678
	11×11	1.5296	1.5351	2.3124	2.3221	2.3085	2.2336	2.2486	2.2092
	17×17	1.9370	2.2557	2.2583	2.2570	2.2487	2.2368	2.2426	2.2220
Analytical (Timoshenko and Woinowsky-Kriger 1959)		2.2528							

Table 2. Material properties used in the FG plates (Neves et al. 2012; Lee, Zhao, and Liew 2009; Li, Ding, et al. 2008).

	Metals		Ceramics			
Mechanical properties	Titanium (Ti)	Aluminum (Al)	Alumina (Al_2O_3)	Zirconia[#] (ZrO_2)	Zirconia[$] ($ZrO_2^{\$}$)	Zirconia[*] (ZrO_2^{*})
E	110.25	70	380	200	278.41	151
ν	0.288	0.3	0.3	0.3	0.288	0.3
ρ	–	2707	3800	5700	–	3000

Table 3. Comparison of the deflection $\overline{w}_c$ of IF square plate Al/ZrO_2 under the uniform loading.

Boundary conditions	a/h	Methods	$\eta = 0$	$\eta = 0.5$	$\eta = 1$	$\eta = 2$
SSSS	5	MK-S-FSDT (Vu et al. 2017)	0.1723	0.2331	0.2723	0.3116
		MK-R-STSDT (Vu et al. 2018a)	0.1721	0.2325	0.2725	0.3142
		Ritz-kp-FSDT (Lee, Zhao, and Liew 2009)	0.1722	0.2403	0.2811	0.3221
		MK-R-ISSDT (Vu et al. 2018c)	0.1749	0.2363	0.2769	0.3193
		MK-N-RSHSDT (Vu, Curiel-Sosa, and Bui 2018b)	0.1773	0.2395	0.2806	0.3238
		Present	0.1728	0.2336	0.2738	0.3159
	100	IGA-S-FSDT (Yin, Yu, and Liu 2013)	0.1423	0.1949	0.2284	0.2597
		MK-R-STSDT (Vu et al. 2018a)	0.1427	0.1954	0.2290	0.2603
		R-SSDT-MK (Vu and Phan 2017)	0.1483	0.2031	0.2379	0.2705
		MK-N-RSHSDT (Vu, Curiel-Sosa, and Bui 2018b)	0.1457	0.1996	0.2339	0.2659
		Present	0.1435	0.1966	0.2304	0.2619
SFSS	5	IGA-S-FSDT (Yin, Yu, and Liu 2013)	0.3164	0.4299	0.5032	0.5752
		MK-R-STSDT (Vu et al. 2018a)	0.3153	0.4278	0.5013	0.5757
		MK-R-ISSDT (Vu et al. 2018c)	0.3181	0.4315	0.5056	0.5808
		MK-N-RSHSDT (Vu, Curiel-Sosa, and Bui 2018b)	0.3233	0.4384	0.5138	0.5902
		Present	0.3162	0.4290	0.5027	0.5775
	100	MK-S-FSDT (Vu et al. 2017)	0.2777	0.3805	0.4458	0.5069
		MK-R-STSDT (Vu et al. 2018a)	0.2766	0.3790	0.4440	0.5047
		MK-N-RSHSDT (Vu, Curiel-Sosa, and Bui 2018b)	0.2816	0.3858	0.4519	0.5138
		Present	0.2776	0.3803	0.4455	0.5064
SFSF	5	IGA-S-FSDT (Yin, Yu, and Liu 2013)	0.5083	0.6918	0.8099	0.9247
		MK-R-STSDT (Vu et al. 2018a)	0.5061	0.6879	0.8061	0.9239
		Ritz-kp-FSDT (Lee, Zhao, and Liew 2009)	0.5061	0.7029	0.8214	0.9423
		MK-R-ISSDT (Vu et al. 2018c)	0.5054	0.6869	0.8048	0.9226
		MK-N-RSHSDT (Vu, Curiel-Sosa, and Bui 2018b)	0.5162	0.7014	0.8219	0.9423
		Present	0.5054	0.6869	0.8048	0.9225
	100	IGA-S-FSDT (Yin, Yu, and Liu 2013)	0.4584	0.6281	0.7360	0.8367
		MK-R-STSDT (Vu et al. 2018a)	0.4564	0.6252	0.7325	0.8327
		R-SSDT-MK (Vu and Phan 2017)	0.4627	0.6339	0.7427	0.8443
		MK-N-RSHSDT (Vu, Curiel-Sosa, and Bui 2018b)	0.4623	0.6333	0.7419	0.8434
		Present	0.4558	0.6243	0.7313	0.8312

$$\mathbf{p}(\mathbf{x}) = \begin{pmatrix} 1 & x & y & x^2 & xy & y^2 \end{pmatrix}^T \tag{33}$$

Furthermore, the 4×4 Gaussian integration is employed for the mechanical behavior analysis of FG plates in this study.

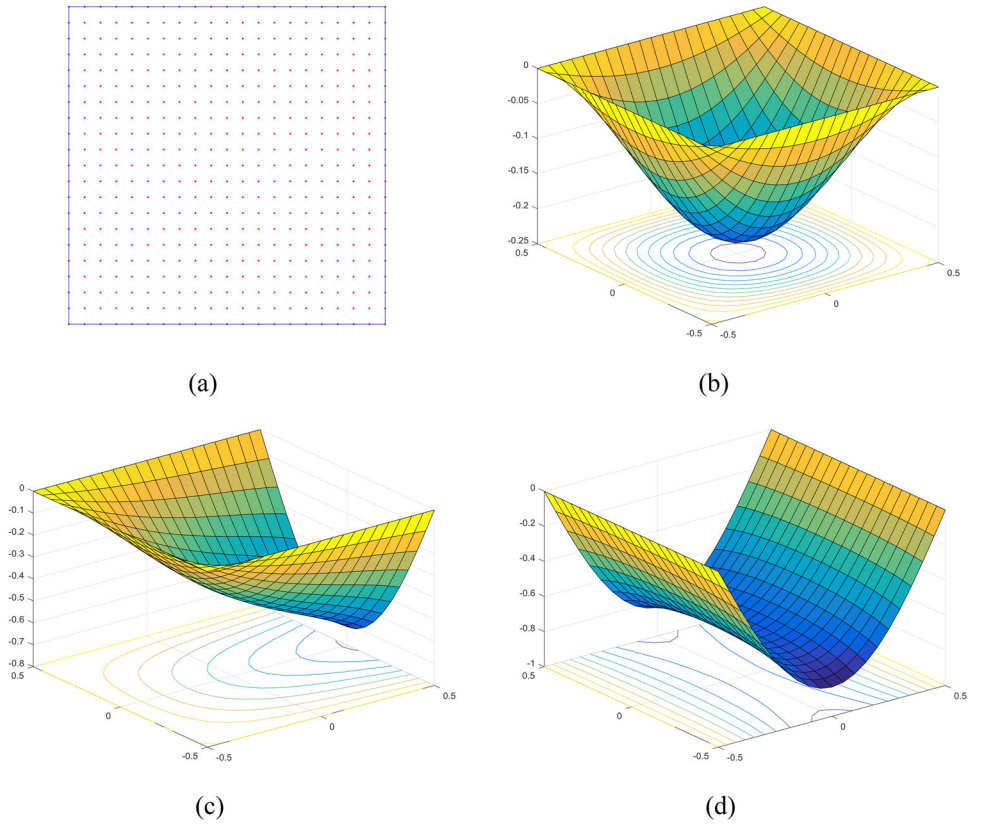

Figure 4. Static bending analysis of IF square plate Al/ZrO_2 by using $\eta = 1$ and $a/h = 100$ under the uniform loading: (a) Nodal distribution, (b) SSSS deformation shape, (c) SFSS deformation shape, (d) SFSF deformation shape.

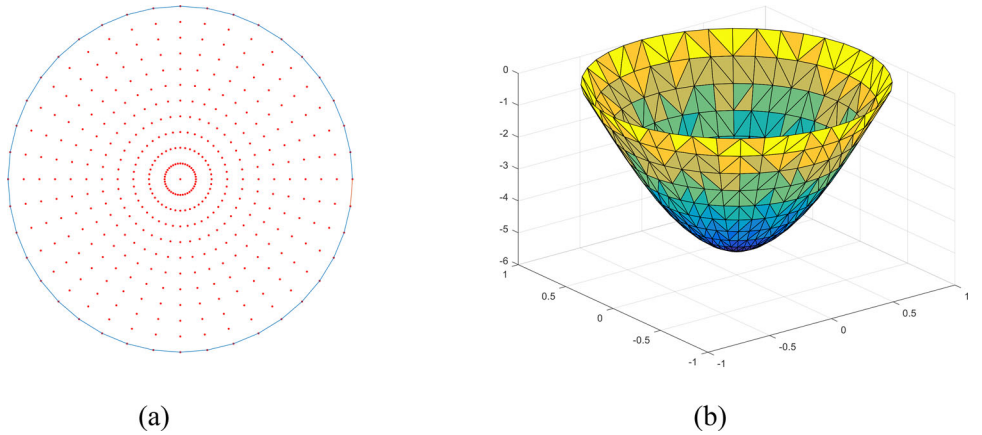

Figure 5. Static bending analysis of the roller supportedAl/ZrO_2 circular plate IF with $\eta = 4$ and $h/R = 0.1$: (a) Uniform nodal distribution, (b) Deformation shape.

4. Numerical results and discussions

In this section, we present our solutions of the static bending, natural frequencies and compressive buckling of FG plates using the rectangular and circular shapes. The boundaries of the plates are defined as the completely free (F), and two Dirichlet types are described below:

Table 4. Comparison of the deflection $\bar{w}_c$ of IF circular plate Ti/ZrO_2^S under uniform loading.

h/R	Methods	$\eta = 0$	$\eta = 2$	$\eta = 4$	$\eta = 8$	$\eta = 10$
(a) Roller boundary						
0.05	Analytical method (Li, Iu, et al. 2008)	10.3910	5.7090	5.2190	4.8090	4.7000
	Semi-analytical method (Reddy, Wang, and Kitipornchai 1999)	10.3960	5.7140	5.2230	4.8120	4.7040
	IGA-HSDT (Tran, Ferreira, and Nguyen-Xuan 2013)	10.2203	5.6100	5.1299	4.7299	4.6239
	IGA-FSDT (Yin et al. 2014)	10.3963	5.7137	5.2227	4.8124	4.7036
	IGA-S-FSDT (Yin et al. 2014)	10.3411	5.4851	5.0966	4.7513	4.6542
	Present	10.3744	5.6213	5.1721	4.7879	4.6839
0.10	Analytical method (Li, Ding, et al. 2008)	10.4600	5.7380	5.2450	4.8350	4.7270
	Semi-analytical method (Reddy, Wang, and Kitipornchai 1999)	10.4810	5.7560	5.2610	4.8480	4.7390
	IGA-HSDT (Tran, Ferreira, and Nguyen-Xuan 2013)	10.3440	5.6742	5.1879	4.7838	4.6769
	IGA-FSDT (Yin et al. 2014)	10.4817	5.7561	5.2612	4.8487	4.7394
	IGA-S-FSDT (Yin et al. 2014)	10.4262	5.5273	5.1349	4.7874	4.6899
	Present	10.4591	5.6622	5.2089	4.8230	4.7186
0.20	Analytical method (Li, Ding, et al. 2008)	10.7360	5.8530	5.3510	4.9410	4.8330
	Semi-analytical method (Reddy, Wang, and Kitipornchai 1999)	10.8220	5.9250	5.4140	4.9930	4.8820
	IGA-HSDT (Tran, Ferreira, and Nguyen-Xuan 2013)	10.6973	5.8475	5.3439	4.9315	4.8230
	IGA-FSDT (Yin et al. 2014)	10.8223	5.9250	5.4147	4.9932	4.8821
	IGA-S-FSDT (Yin et al. 2014)	10.7667	5.6961	5.2883	4.9319	4.8326
	Present	10.8000	5.8273	5.3573	4.9640	4.8585
(b) Clamped boundary						
0.05	Analytical method (Li, Ding, et al. 2008)	2.5610	1.4050	1.2840	1.1840	1.1570
	Semi-analytical method (Reddy, Wang, and Kitipornchai 1999)	2.5540	1.4020	1.2820	1.1810	1.1550
	IGA-HSDT (Tran, Ferreira, and Nguyen-Xuan 2013)	2.5480	1.3990	1.2786	1.1785	1.1520
	IGA-FSDT (Yin et al. 2014)	2.5539	1.4024	1.2819	1.1814	1.1547
	IGA-S-FSDT (Yin et al. 2014)	2.5535	1.4023	1.2817	1.1812	1.1546
	Present	2.5562	1.3965	1.2792	1.1809	1.1547
0.10	Analytical method (Li, Ding, et al. 2008)	2.6670	1.4560	1.3290	1.2270	1.2010
	Semi-analytical method (Reddy, Wang, and Kitipornchai 1999)	2.6390	1.4440	1.3200	1.2170	1.1900
	IGA-HSDT (Tran, Ferreira, and Nguyen-Xuan 2013)	2.6297	1.4386	1.3143	1.2123	1.1855
	IGA-FSDT (Yin et al. 2014)	2.6393	1.4448	1.3203	1.2176	1.1905
	IGA-S-FSDT (Yin et al. 2014)	2.6353	1.4428	1.3186	1.2159	1.1889
	Present	2.6410	1.4375	1.3160	1.2160	1.1895
0.20	Analytical method (Li, Ding, et al. 2008)	3.0930	1.6580	1.5110	1.4020	1.3750
	Semi-analytical method (Reddy, Wang, and Kitipornchai 1999)	2.9790	1.6130	1.4730	1.3620	1.3330
	IGA-HSDT (Tran, Ferreira, and Nguyen-Xuan 2013)	2.9541	1.5958	1.4557	1.3467	1.3187
	IGA-FSDT (Yin et al. 2014)	2.9799	1.6137	1.4738	1.3622	1.3332
	IGA-S-FSDT (Yin et al. 2014)	2.9625	1.6051	1.4659	1.3548	1.3260
	Present	2.9814	1.6023	1.4642	1.3568	1.3291

(i) Simply-supported boundary condition (S):

$$w_b(x,y) = w_s(x,y) = 0 \text{ at } x = 0, a \text{ and } y = 0, b \tag{34}$$

(ii) Clamped boundary condition (C):

$$\begin{aligned} &w_b(x,y) = w_s(x,y) = 0 \\ &\partial w_b(x,y)/\partial n = \partial w_s(x,y)/\partial n = 0 \text{ at } x = 0, a \text{ and } y = 0, b \end{aligned} \tag{35a, 35b}$$

Due to the MKI shape functions possessed Kronecker delta property, the boundary conditions of $w_b(x,y), w_s(x,y)$ can be enforced as the FEM. The normal slope $\partial w_b(x,y)/\partial n, \partial w_s(x,y)/\partial n$ can be imposed as the bending strip method (Kiendl et al. 2010) wherein the transverse displacements of both the adjacent and boundary nodes were assigned by zero values as shown in Figure 3.

Table 5. Comparison of the deflection $\bar{w}_c$ of FCHS square plate Al/Al_2O_3 with the layer ratio of $(2/1/2)$ under bi-sinusoidal loading.

a/h	Methods	$\eta = 0$	$\eta = 1$	$\eta = 4$	$\eta = 7$	$\eta = 10$
4	CLT (Carrera et al. 2011)	–	0.6070	0.7792	–	0.8070
	FSDT (Carrera et al. 2011)	–	0.7738	1.0285	–	1.1109
	CUF (Carrera et al. 2011)	–	0.7735	1.0977	–	1.2240
	HSDT (Neves et al. 2013)	–	0.7746	1.0826	–	1.2183
	MK-R-ISSDT (Vu et al. 2018c)	0.4647	0.7751	1.0897	1.1826	1.2259
	MK-N-RSHSDT (Vu, Curiel-Sosa, and Bui 2018b)	0.4639	0.7725	1.0934	1.1896	1.2320
	Present	0.4659	0.7771	1.0965	1.1917	1.2353
10	CLT (Carrera et al. 2011)	–	0.6070	0.7792	–	0.8070
	FSDT (Carrera et al. 2011)	–	0.6337	0.8191	–	0.8556
	CUF (Carrera et al. 2011)	–	0.6337	0.8308	–	0.8743
	HSDT (Neves et al. 2013)	–	0.6357	0.8272	–	0.8712
	MK-R-ISSDT (Vu et al. 2018c)	0.3764	0.6359	0.8311	0.8624	0.8767
	MK-N-RSHSDT (Vu, Curiel-Sosa, and Bui 2018b)	0.3763	0.6355	0.8318	0.8637	0.8779
	Present	0.3776	0.6383	0.8352	0.8669	0.8813
100	CLT (Carrera et al. 2011)	–	0.6070	0.7792	–	0.8070
	FSDT (Carrera et al. 2011)	–	0.6073	0.7796	–	0.8075
	CUF (Carrera et al. 2011)	–	0.6072	0.7797	–	0.8077
	HSDT (Neves et al. 2013)	–	0.6092	0.7785	–	0.8050
	MK-R-ISSDT (Vu et al. 2018c)	0.3597	0.6095	0.7819	0.8015	0.8103
	MK-N-RSHSDT (Vu, Curiel-Sosa, and Bui 2018b)	0.3597	0.6095	0.7819	0.8015	0.8103
	Present	0.3609	0.6120	0.7855	0.8050	0.8138

Table 6. Comparison of the deflection $\breve{w}_c$ of HCFS square plate $Al/ZrO_2 - 3$ with all SSSS edges and $a/h = 10$ under bi-sinusoidal loading.

Schemes of HCFS	Methods	$\eta = 0$	$\eta = 0.5$	$\eta = 1$	$\eta = 2$	$\eta = 5$	$\eta = 10$
$(2/1/2)$	CLT (Neves et al. 2012)	0.1856	–	0.2942	0.3394	0.3779	0.3894
	FSDT (Neves et al. 2012)	0.1961	–	0.3075	0.3541	0.3942	0.4066
	HSDT (Bessaim et al. 2013)	0.1949	0.2614	0.3043	0.3500	0.3893	0.4015
	ZZF (Neves et al. 2012)	0.1961	0.2667	0.3090	0.3542	0.3930	0.4051
	MK-N-RSHSDT (Vu, Curiel-Sosa, and Bui 2018b)	0.1970	0.2644	0.3078	0.3539	0.3935	0.4058
	Present	0.1976	0.2652	0.3087	0.3549	0.3946	0.4068
$(2/1/1)$	CLT (Neves et al. 2012)	–	–	–	–	–	–
	FSDT (Neves et al. 2012)	–	–	–	–	–	–
	HSDT (Bessaim et al. 2013)	0.1949	0.2560	0.2945	0.3350	0.3698	0.3811
	ZZF (Neves et al. 2012)	0.1961	0.2614	0.2995	0.3399	0.3746	0.3861
	MK-N-RSHSDT (Vu, Curiel-Sosa, and Bui 2018b)	0.1970	0.2590	0.2982	0.3394	0.3748	0.3862
	Present	0.1976	0.2598	0.2991	0.3404	0.3759	0.3873
$(1/1/1)$	CLT (Neves et al. 2012)	0.1856	–	0.2803	0.3207	0.3587	0.3724
	FSDT (Neves et al. 2012)	0.1961	–	0.2930	0.3344	0.3736	0.3879
	HSDT (Bessaim et al. 2013)	0.1949	0.2530	0.2901	0.3307	0.3690	0.3830
	ZZF (Neves et al. 2012)	0.1961	0.2583	0.2949	0.3351	0.3729	0.3868
	MK-N-RSHSDT (Vu, Curiel-Sosa, and Bui 2018b)	0.1970	0.2559	0.2934	0.3345	0.3731	0.3872
	Present	0.1976	0.2566	0.2943	0.3354	0.3742	0.3883
$(2/2/1)$	CLT (Neves et al. 2012)	0.1856	–	0.2692	0.3041	0.3369	0.3492
	FSDT (Neves et al. 2012)	0.1961	–	0.2817	0.3174	0.3512	0.3640
	HSDT (Bessaim et al. 2013)	0.1949	0.2466	0.2787	0.3136	0.3465	0.3589
	ZZF (Neves et al. 2012)	0.1961	0.2519	0.2838	0.3186	0.3514	0.3637
	MK-N-RSHSDT (Vu, Curiel-Sosa, and Bui 2018b)	0.1970	0.2495	0.2822	0.3177	0.3512	0.3638
	Present	0.1976	0.2502	0.2831	0.3186	0.3523	0.3648
	CLT (Neves et al. 2012)	0.1856	–	0.2596	0.2910	0.3228	0.3361
	FSDT (Neves et al. 2012)	0.1961	–	0.2717	0.3037	0.3363	0.3500
	HSDT (Bessaim et al. 2013)	0.1949	0.2407	0.2692	0.3006	0.3326	0.3459
$(1/2/1)$	ZZF (Neves et al. 2012)	0.1961	0.2460	0.2740	0.3053	0.3370	0.3503
	MK-N-RSHSDT (Vu, Curiel-Sosa, and Bui 2018b)	0.1970	0.2435	0.2723	0.3041	0.3364	0.3499
	Present	0.1976	0.2443	0.2731	0.3051	0.3374	0.3509

Table 7. Comparison of the first five normalized frequencies $\overline{\omega}$ of IF square Al/Al_2O_3 plate with $a/h = 100$.

η	Methods	$\overline{\omega}_1$	$\overline{\omega}_2$	$\overline{\omega}_3$	$\overline{\omega}_4$	$\overline{\omega}_5$
(a) SFSF						
1	IGA-neu-CPT (Yin, Yu, and Liu 2013)	43.1596	72.2984	164.5401	174.5012	209.4085
	MK-S-FSDT (Vu et al. 2017)	43.2374	71.2856	161.2857	175.8363	206.5470
	Exact (Baferani, Saidi, and Jomehzadeh 2011)	43.0872	72.2001	164.3911	–	–
	MK-N-RSHSDT(Vu, Curiel-Sosa, and Bui 2018b)	42.9806	71.7756	162.0638	171.5960	204.8737
	Present	43.3645	72.5290	164.2374	176.9646	211.7085
2	IGA-neu-CPT (Yin, Yu, and Liu 2013)	39.2395	65.7314	149.5922	158.6496	190.3849
	MK-S-FSDT (Vu et al. 2017)	39.3354	64.9015	146.9400	160.1133	188.3231
	Exact (Baferani, Saidi, and Jomehzadeh 2011)	39.1666	65.6400	149.0583	–	–
	MK-N-RSHSDT(Vu, Curiel-Sosa, and Bui 2018b)	39.0828	65.2660	147.3546	156.0896	186.3556
	Present	39.4466	65.9652	149.3606	161.1708	192.7461
(b) SSSS						
1	IGA-neu-CPT (Yin, Yu, and Liu 2013)	88.4501	221.1011	221.1011	353.7127	442.1697
	MK-S-FSDT (Vu et al. 2017)	88.4983	223.1878	223.1878	359.3324	448.5040
	Exact (Baferani, Saidi, and Jomehzadeh 2011)	88.3093	221.0643	–	353.6252	–
	MK-N-RSHSDT(Vu, Curiel-Sosa, and Bui 2018b)	87.4004	215.2458	215.2458	337.5635	421.0957
	Present	88.0741	220.6463	220.6463	348.1155	445.8387
2	IGA-neu-CPT (Yin, Yu, and Liu 2013)	80.4160	201.0155	201.0155	321.5761	401.9929
	MK-S-FSDT (Vu et al. 2017)	80.6550	204.0120	204.0120	330.2422	411.6235
	Exact (Baferani, Saidi, and Jomehzadeh 2011)	80.3517	200.8793	–	321.4069	–
	MK-N-RSHSDT(Vu, Curiel-Sosa, and Bui 2018b)	79.4630	195.7338	195.7338	306.9145	383.1018
	Present	80.0823	200.7826	200.7826	316.6364	406.4149
(c) SCSC						
1	IGA-neu-CPT (Yin, Yu, and Liu 2013)	129.7269	245.2758	310.6242	423.7400	457.9482
	MK-S-FSDT (Vu et al. 2017)	129.9227	246.0544	311.5795	429.6741	456.0445
	Exact (Baferani, Saidi, and Jomehzadeh 2011)	129.6496	245.1310	–	423.6904	–
	MK-N-RSHSDT(Vu, Curiel-Sosa, and Bui 2018b)	129.2264	239.9096	305.1543	408.8027	438.4519
	Present	129.5006	242.8763	304.7069	415.8221	447.8102
2	IGA-neu-CPT (Yin, Yu, and Liu 2013)	117.9435	222.9939	282.4052	385.2402	416.3375
	MK-S-FSDT (Vu et al. 2017)	117.9340	223.2098	279.5867	389.7883	412.6522
	Exact (Baferani, Saidi, and Jomehzadeh 2011)	117.8104	222.8111	–	385.0672	–
	MK-N-RSHSDT(Vu, Curiel-Sosa, and Bui 2018b)	117.5411	218.2121	277.5496	371.8758	398.9104
	Present	117.8349	220.9597	277.4365	378.5907	407.4546
(d) CCCC						
1	IGA-neu-CPT (Yin, Yu, and Liu 2013)	161.2484	328.8502	328.8502	484.8293	589.5860
	MK-S-FSDT (Vu et al. 2017)	161.0227	328.6780	328.6780	488.7393	591.5320
	MK-N-RSHSDT(Vu, Curiel-Sosa, and Bui 2018b)	160.8461	322.9511	322.9511	467.6309	564.5060
	Present	160.8862	322.6883	322.6883	474.1163	566.4382
2	IGA-neu-CPT (Yin, Yu, and Liu 2013)	146.6016	298.9753	298.9753	440.7781	536.0119
	MK-S-FSDT (Vu et al. 2017)	146.9611	297.6900	297.6900	441.7803	531.8659
	MK-N-RSHSDT(Vu, Curiel-Sosa, and Bui 2018b)	146.3175	293.7530	293.7530	425.4270	513.5280
	Present	146.4105	293.7948	293.7948	431.7738	516.0873

4.1. Convergence study and effect of the scaling factor on solution accuracy

Consider a full-simply supported homogeneous square plate with the length to thickness ratio $a/h = 100$ and the length of side $a = 1.0m$, subjected to the uniform traction $\overline{q}_0 = 1.0N/m^2$. Plate material properties are given as follows: Young's modulus $E_m = 2.0GPa$, Poisson's ratio $\nu = 0.3$ The analytical solution for bending of this Kirchhoff's plate is provided by Timoshenko and Woinowsky-Kriger (1959).

$$w(x,y) = \frac{16\overline{q}_0}{D\pi^6}\sum_{m=1}^{\infty}\sum_{n=1}^{\infty}\frac{\sin(m\pi x/a)\sin(m\pi y/a)}{mn\left((m/a)^2+(n/a)^2\right)^2} \tag{36}$$

where m, n are odd numbers, and $D = \frac{Eh^3}{12(1-\nu^2)}$. The convergence of the analytical solution is so fast, thus the central deflection can be estimated with $m = n = 5$ by $\overline{w}_c = 2.2528 \times 10^{-3}m$. To investigate the influence of scaling factor to numerical solution accuracy, different node patterns of 5×5, 7×7, 9×9, 11×11 and 17×17 combined with varying scaling factors, the obtained results are given in Table 1. For the value of scaling factor greater than 2, it can be seen that all

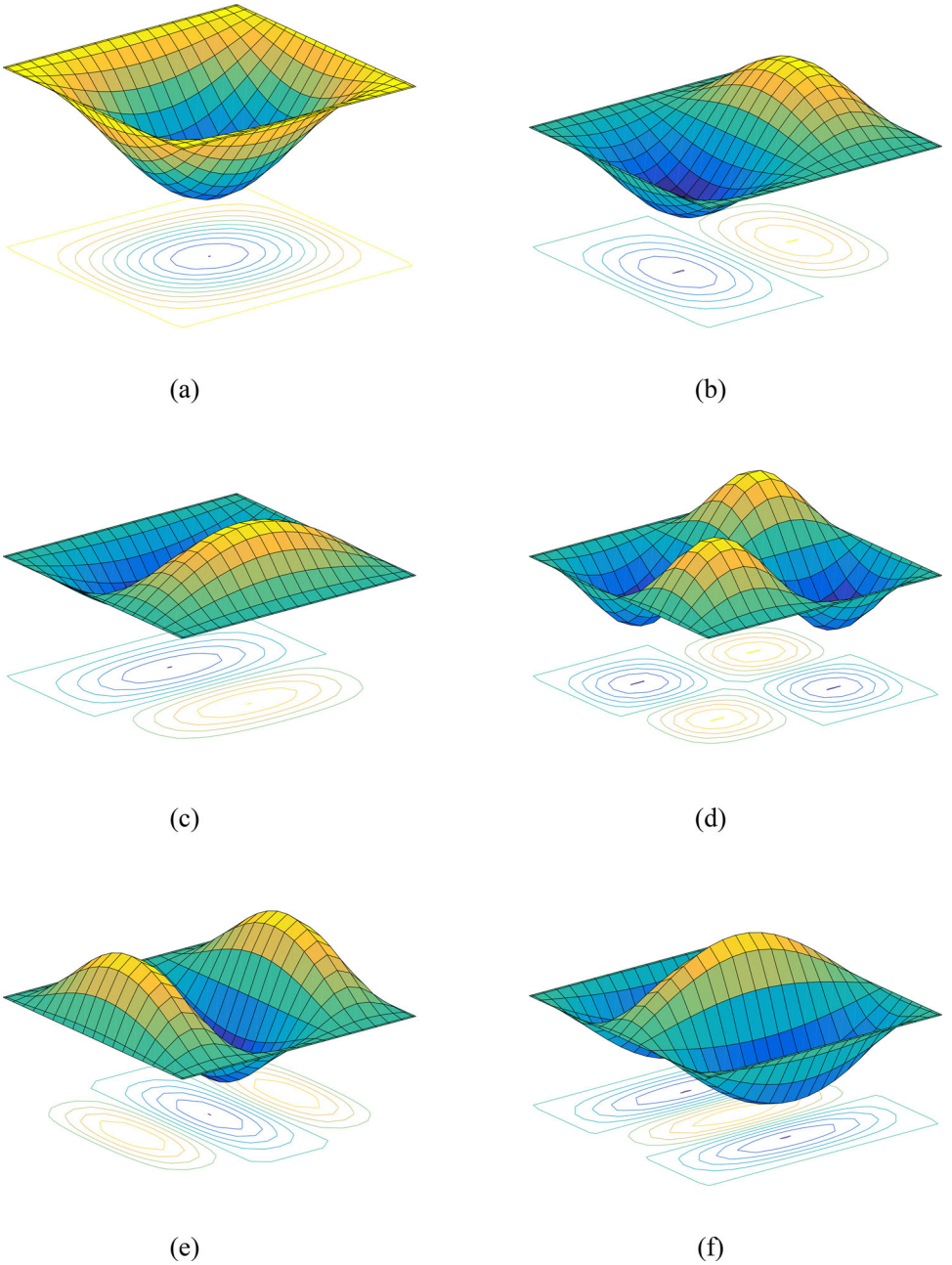

Figure 6. Natural frequency analysis of the SCSC Al/Al_2O_3 square plate IF with $\eta = 1$ and $a/h = 100$: (a) Mode shape 1, (b) Mode shape 2, (c) Mode shape 3, (d) Mode shape 4, (e) Mode shape 5, (f) Mode shape 6.

the results converged to the exact solution as number of discrete nodes increases showing that the quadric correlation function can ensure the stable numerical solution. Furthermore, the deflection is convergent to the exact deflection as scaling factor $2 < \alpha \leq 3.5$. As $\alpha > 3.5$, the good result could not be obtained due to the density of distribution nodes inside the influence domains may be too dense. However, when $\alpha < 2$, the matrix $\hat{\mathbf{A}}$ in Eq. (10a) is closely singular or badly scaled, as a result that problem could not be solved or hardly reaches a good solution. Thus, we consider that a value of $\alpha = 2.10$ for numerical analysis in the following computations.

Table 8. Comparison of the first six normalized frequencies $\tilde{\omega}$ of IF circular plate Al/Al_2O_3 with clamped periphery and gradient index $\eta = 1$.

h/R	Methods	$\tilde{w}_1$	$\tilde{w}_2$	$\tilde{w}_3$	$\tilde{w}_4$	$\tilde{w}_5$	$\tilde{w}_6$
0.01	Semi-analytical-FSDT (Hosseini-Hashemi, Fadaee, and Es'haghi 2010)	0.0236	0.0491	0.0805	0.0918	0.1178	0.1404
	FEM-UM (Ebrahimi, Rastgoo, and Atai 2009)	0.0234	0.0486	0.0798	0.0909	0.1167	0.1391
	UM-FSDT (Ebrahimi, Rastgoo, and Atai 2009)	0.0257	0.0535	0.0877	0.1000	0.1283	0.1529
	IGA-HSDT (Tran, Ferreira, and Nguyen-Xuan 2013)	0.0236	0.0492	0.0807	0.0924	0.1191	0.1431
	IGA-FSDT (Yin et al. 2014)	0.0237	0.0511	0.0855	0.0997	0.1101	0.1451
	IGA-S-FSDT (Yin et al. 2014)	0.0236	0.0491	0.0805	0.0919	0.1180	0.1408
	Present	0.0238	0.0499	0.0808	0.0914	0.1176	0.1400
0.10	Semi-analytical-FSDT(Hosseini-Hashemi, Fadaee, and Es'haghi 2010)	2.3053	4.6934	7.5146	8.5181	10.7128	12.6197
	FEM-UM (Ebrahimi, Rastgoo, and Atai 2009)	2.2888	4.6661	7.4808	8.4829	10.6776	12.5877
	UM-FSDT (Ebrahimi, Rastgoo, and Atai 2009)	2.5038	5.0831	8.1156	9.1931	11.5376	13.5743
	IGA-HSDT (Tran, Ferreira, and Nguyen-Xuan 2013)	2.3076	4.7005	7.5318	8.5380	10.7483	12.6636
	IGA-FSDT (Yin et al. 2014)	2.3042	4.6936	7.5190	8.5472	10.7923	12.8097
	IGA-S-FSDT (Yin et al. 2014)	2.3040	4.7137	7.5773	8.5244	10.8524	12.7017
	Present	2.3200	4.7800	7.5916	8.4462	10.7941	12.5870
0.20	Semi-analytical-FSDT (Hosseini-Hashemi, Fadaee, and Es'haghi 2010)	8.6535	16.7666	25.6486	28.7574	34.0756	35.0981
	FEM-UM (Ebrahimi, Rastgoo, and Atai 2009)	8.6403	16.7890	25.7661	28.9152	34.1893	35.3618
	UM-FSDT (Ebrahimi, Rastgoo, and Atai 2009)	9.3162	17.9164	27.2480	30.4998	–	37.1197
	IGA-HSDT (Tran, Ferreira, and Nguyen-Xuan 2013)	8.6787	16.8595	25.8479	29.0092	34.0581	35.4875
	IGA-FSDT (Yin et al. 2014)	8.6490	16.7604	25.6426	28.7732	34.0571	35.1592
	IGA-S-FSDT (Yin et al. 2014)	8.6486	17.0016	26.2512	28.7691	34.1216	36.1557
	Present	8.7053	17.2065	26.2941	28.4795	33.1921	35.9974

4.2. Static bending of the FG plates

Firstly, we consider an IF square Al/ZrO_2 plate with the different boundaries of SSSS, SFSS, SFSF and having side-to-thickness ratios a/h of 5, 100 and subjected to the uniform loading.

Its constituent materials shown in Table 2, and material properties continuously change according to Eq. (1). Table 3 shows the non-dimensional central deflection $\overline{w}_c = \frac{100E_m h^3}{12(1-\upsilon_m^2)q_0 a^4} w\left(\frac{a}{2}, \frac{b}{2}, 0\right)$ by using the gradient indices η by $0, 0.5, 1$ and 2 with a fine mesh of 21×21 nodes as shown in Figure 4a. In studying Table 3, it is clear that the present results are in good agreement with solutions obtained by many available methods such as the refined plate theory combined with the MKI method such as: MK-S-FSDT (Vu et al. 2017); R-SSDT-MK (Vu and Phan 2017); MK-R-STSDT (Vu et al. 2018a); MK-N-RSHSDT (Vu, Curiel-Sosa, and Bui 2018b); MK-R-ISSDT (Vu et al. 2018c) and IGA-S-FSDT (Yin, Yu, and Liu 2013), Ritz-kp-FSDT (Lee, Zhao, and Liew 2009) method.

Due to the FG plate stiffness, increasing when its boundary conditions vary from SFSF, SFSS to SSSS or the ratio a/h increase from 5 to 100, it leads to a reduction of the plate central deflection. In contrast, increasing the value of gradient index η gains, an increase in the deflection magnitudes since the plate material properties approximated to those of metal component.

It should be noted that the effect of the transverse shear deformation in the plate-bending behavior of the thin plates is smaller than those from thick plates. As the result, the deflections for the thinner plate (e.g., $a/h = 100$) are smaller than those of the thicker plate (e.g., $a/h = 5$). Figure 4b–d depict the plate deformed shapes by using the various boundary conditions under the uniformly distributed load. Next, we analysis the static bending of an IF circular $Ti/ZrO_2^{\$}$ plate subjected the uniformly distributed load with considering the roller and clamped boundaries along its periphery. Circle plate material properties are determined by the mixture rule by Eq. (37) as follows:

$$P_e = P_c V_c(z) + P_m V_m(z) \;\; where \;\; V_m(z) = (1/2 - z/h)^{\eta}, \;\; V_c(z) = 1 - V_m(z) \qquad (37a, 37b, 37c)$$

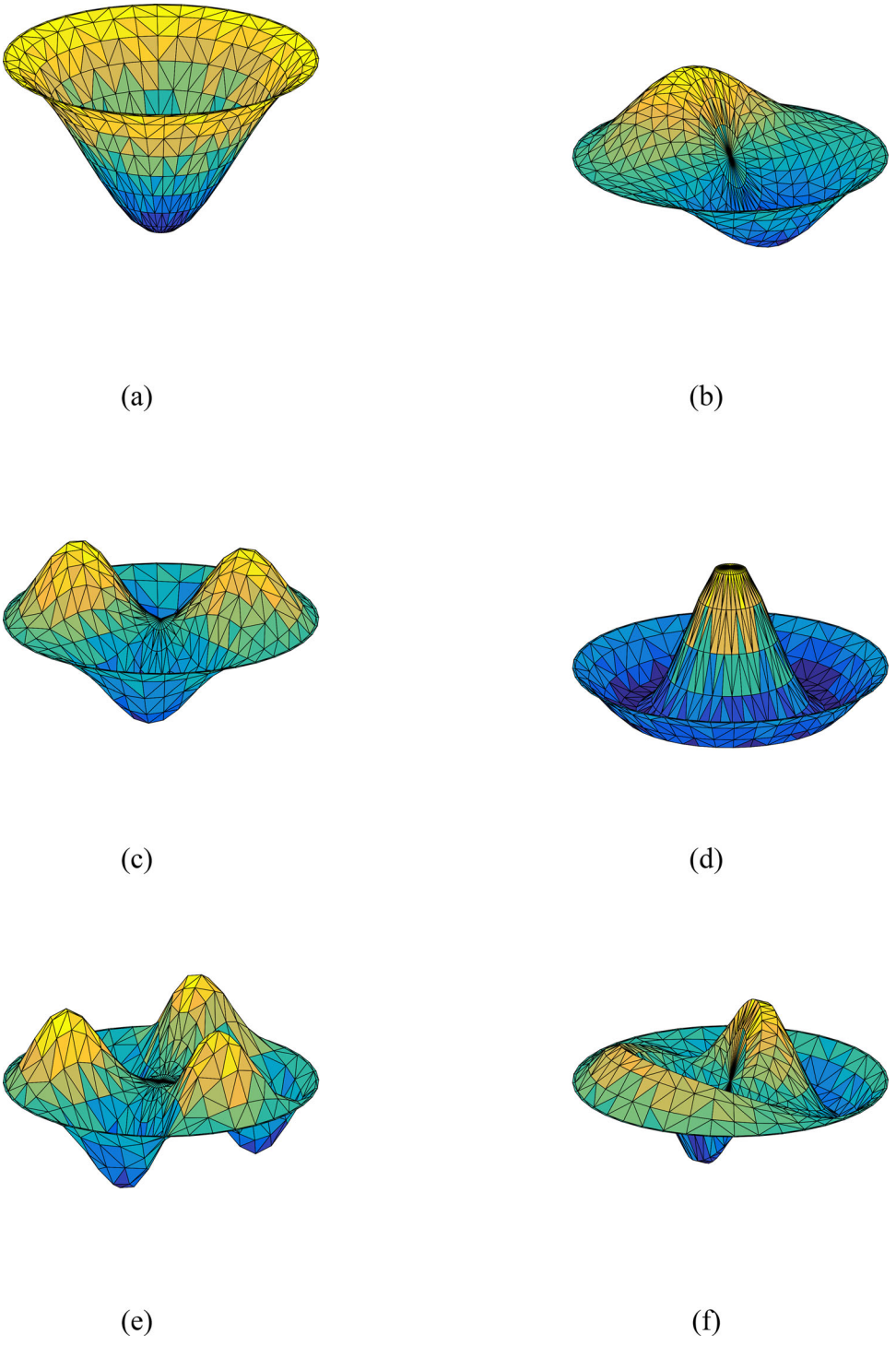

Figure 7. Natural frequency analysis of the clamped Al/Al_2O_3 circular plate (IF) with $\eta = 1$ and $a/h = 100$: (a) Mode shape 1, (b) Mode shape 2, (c) Mode shape 3, (d) Mode shape 4, (e) Mode shape 5, (f) Mode shape 6.

Table 9. Comparison of the first frequency $\tilde{w}_1$ of IF circular plate Al/Al_2O_3 with $h/R = 0.01$.

Boundary conditions	Methods	$\eta = 0$	$\eta = 1$	$\eta = 2$	$\eta = 5$	$\eta = 10$
Free	IGA-FSDT (Yin et al. 2014)	0.0162	0.0124	0.0113	0.0107	0.0103
	IGA-S-FSDT (Yin et al. 2014)	0.0162	0.0123	0.0112	0.0106	0.0103
	Present	0.0162	0.0124	0.0113	0.0107	0.0103
Roller	IGA-FSDT (Yin et al. 2014)	0.0150	0.0114	0.0104	0.0098	0.0095
	IGA-S-FSDT (Yin et al. 2014)	0.0150	0.0121	0.0114	0.0107	0.0100
	Present	0.0150	0.0122	0.0115	0.0108	0.0101
Clamped	IGA-FSDT (Yin et al. 2014)	0.0311	0.0237	0.0216	0.0204	0.0198
	IGA-S-FSDT (Yin et al. 2014)	0.0309	0.0236	0.0214	0.0203	0.0197
	Present	0.0309	0.0236	0.0215	0.0204	0.0196

Table 10. Comparison of the first five frequencies $\tilde{\omega}$ of FCHS square plates Al/Al_2O_3 with a layer ratio of 1/8/1 using $\eta = 1$ and $(a/h = 100, 10)$.

a/h	Methods	$\tilde{\omega}_1$	$\tilde{\omega}_2$	$\tilde{\omega}_3$	$\tilde{\omega}_4$	$\tilde{\omega}_5$
(a) SSSS						
100	Ritz-3D (Li, lu, et al. 2008)	1.5760	3.9379	3.9379	6.2972	7.8686
	MK-N-RSHSDT (Vu, Curiel-Sosa, and Bui 2018b)	1.5649	3.9048	3.9048	6.2115	7.7989
	Present	1.5625	3.9092	3.9092	6.1711	7.8760
10	Ritz-3D (Li, lu, et al. 2008)	1.5221	3.6295	3.6295	5.5679	6.7829
	MK-N-RSHSDT (Vu, Curiel-Sosa, and Bui 2018b)	1.5123	3.6037	3.6037	5.5046	6.7337
	Present	1.5102	3.6075	3.6075	5.4736	6.7861
(b) CCCC						
100	Ritz-3D (Li, lu, et al. 2008)	2.8830	5.8720	5.8720	8.6495	10.5180
	MK-N-RSHSDT (Vu, Curiel-Sosa, and Bui 2018b)	2.7942	5.6682	5.6682	8.2370	10.1953
	Present	2.8498	5.7108	5.7108	8.3863	10.0113
10	Ritz-3D (Li, lu, et al. 2008)	2.6050	4.9630	4.9630	6.9516	8.1872
	MK-N-RSHSDT (Vu, Curiel-Sosa, and Bui 2018b)	2.5673	4.9431	4.9431	6.9022	8.1657
	Present	2.6101	4.9683	4.9683	6.9852	8.1459

The normalized deflection $\tilde{w}_c = \frac{64D_c}{q_0R^4} w(0,0,0)$ with $D_c = E_c h^3/12(1-\nu_c^2)$ in the center of the plate is calculated using a set of 145 points (see Figure 5a) with respect to the thickness-to-radius ratios $h/R = 0.05,\ 0.1$ and 0.2, are gathered in Table 4.

From the table results, it can be concluded that present solutions are in good agreement with those obtained by IGA-S-FSDT, IGA-FSDT (Yin et al. 2014) and IGA-HSDT (Tran, Ferreira, and Nguyen-Xuan 2013), analytical- (Li, Ding, et al. 2008) and semi-analytical method (Reddy, Wang, and Kitipornchai 1999). The deflection shape of the plate is also plotted in Figure 5b. It can be observed that its deflection pattern is similar to the above square plate. We further consider a FCHS square plate with the ratio $a/h = 10$ and SSSS at all edges. Its bottom skin of the plate is aluminum and top skin is alumina, both skins have the same thickness $0.1h$. Material properties of the core changing from aluminum to alumina are determined by Eq. (1). The plate material properties vary across the thickness direction are calculated by Eq. (2). The top surface of the plate is subjected by a bi-sinusoidal transverse load $q_0 = \overline{q}_0 \sin(\pi x/a)\sin(\pi y/b)$. The computed normalized central displacement $\widehat{w}_c = \frac{10E_c h^3}{\overline{q}_0 a^4} w\left(\frac{a}{2}, \frac{b}{2}, 0\right)$ is compared with the numerical solutions based on the CPT (Carrera et al. 2011), FSDT (Carrera et al. 2011), HSDT (Neves et al. 2013) and CUF (Carrera et al. 2011) methods and listed in Table 5.

Well agreement is evident with those based on the different plate theories with and without using the shear correction factor. It is noteworthy that increasing the value of gradient index η gains the flexural rigidity of the plate is increasing due to the effective material of the FCHS plates come close to those of ceramic component, as the result, the deflection magnitudes are decrease.

Finally, in order to validate our proposed method based on RAESDT for FG sandwich under different layer ratios, on all SSSS edges Al/ZrO_2^* square plate with type HCFS and the ratio

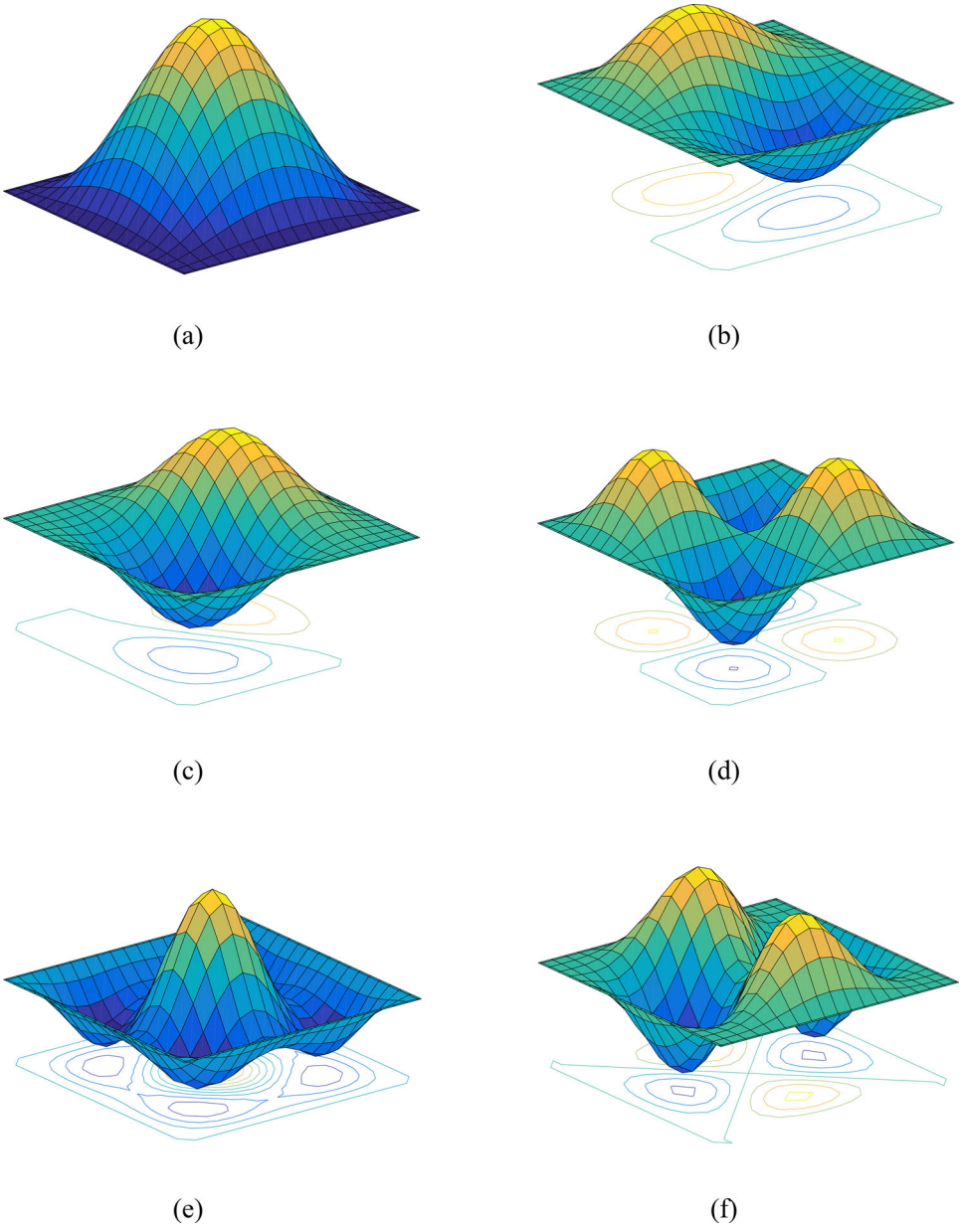

Figure 8. Natural frequency analysis of the CCCC sandwich square plate FCHS with $(1/8/1), \eta = 1$ and $a/h = 10$: (a) Mode shape 1, (b) Mode shape 2, (c) Mode shape 3, (d) Mode shape 4, (e) Mode shape 5, (f) Mode shape 6.

$a/h = 10$ subjected to the bi-sinusoidal force. Mechanical properties of each constituent are shown in Table 2. The plate core skin is a fully ceramic. The variation of the material properties across the plate thickness are determined by Eq. (3). Table 6 shows the central deflection normalized by $\breve{w}_c = \frac{10E_o h}{\bar{q}_0 a^2} w\left(\frac{a}{2}, \frac{b}{2}, 0\right)$, where $q_0 = 1$ and $E_0 = 1$ with different values of gradient index η and layer ratios.

Present RAESDT results are compared with the CLT analytical solutions, FSDT analytical solutions (Neves et al. 2012), HSDT analytical solutions (Bessaim et al. 2013) and ZZF (Neves et al. 2012) meshless solutions (Bessaim et al. 2013), and MK-RSHSDT (Vu, Curiel-Sosa, and Bui

Table 11. Comparison of the first frequencies $\bar{\omega}_1$ of HCFS square plates Al/Al_2O_3 with the SSSS boundary condition and $a/h = 10$ using different layer ratios and gradient indices.

		Layer ratios of plate HCFS					
η	Methods	(1/0/1)	(2/1/2)	(2/1/1)	(1/1/1)	(2/2/1)	(1/2/1)
0.5	Ritz-3D (Li, lu, et al. 2008)	1.4461	1.4861	1.5084	1.5213	1.5493	1.5766
	SSDT (Zenkour 2005)	1.4443	1.4842	1.5126	1.5193	1.5520	1.5745
	TSDT (Zenkour 2005)	1.4442	1.4842	1.5125	1.5192	1.5520	1.5745
	MK-N-RSHSDT(Vu, Curiel-Sosa, and Bui 2018b)	1.4406	1.5027	1.5026	1.5153	1.5432	1.5704
	Present	1.4386	1.4782	1.5004	1.5131	1.5409	1.5680
1	Ritz-3D (Li, lu, et al. 2008)	1.2447	1.3018	1.3351	1.3552	1.3976	1.4413
	SSDT (Zenkour 2005)	1.2433	1.3002	1.3489	1.3534	1.4079	1.4393
	TSDT (Zenkour 2005)	1.2432	1.3001	1.3489	1.3533	1.4079	1.4393
	MK-N-RSHSDT(Vu, Curiel-Sosa, and Bui 2018b)	1.2402	1.2969	1.3301	1.3499	1.3921	1.4355
	Present	1.2384	1.2950	1.3281	1.3479	1.3900	1.4334
5	Ritz-3D (Li, lu, et al. 2008)	0.9448	0.9810	1.0294	1.0453	1.1098	1.1757
	SSDT (Zenkour 2005)	0.9463	0.9820	1.0744	1.0448	1.1474	1.1740
	TSDT (Zenkour 2005)	0.9460	0.9818	1.0743	1.0447	1.1473	1.1740
	MK-N-RSHSDT(Vu, Curiel-Sosa, and Bui 2018b)	0.9439	0.9796	1.0283	1.0421	1.1064	1.1709
	Present	0.9427	0.9783	1.0267	1.0406	1.1047	1.1692
10	Ritz-3D (Li, lu, et al. 2008)	0.9273	0.9418	0.9893	0.9952	1.0610	1.1247
	SSDT (Zenkour 2005)	0.9288	0.9433	1.0455	0.9952	1.0415	1.1346
	TSDT (Zenkour 2005)	0.9284	0.9430	1.0386	0.9955	1.1053	1.1231
	MK-N-RSHSDT(Vu, Curiel-Sosa, and Bui 2018b)	0.9265	0.9409	0.9900	0.9932	1.0587	1.1203
	Present	0.9253	0.9396	0.9884	0.9918	1.0570	1.1186

2018b) meshless solutions. From Table 6, it is evident that the present results agree well with those indicated in the literature (Neves et al. 2012; Bessaim et al. 2013; Vu, Curiel-Sosa, and Bui 2018b) for all plate layer ratios with different gradient indices. It can be concluded that the present RAESDT with meliorated MKI meshless method can accurately solve the static bending problems of FG plates with the different plate shapes and boundary conditions under various loads. It should be mentioned that increasing the core thickness of the HCFS plate gains the flexural rigidity of the plate is increasing, as the result, the deflection amplitudes of the plate are decrease. Conversely, increasing the skin thickness of the HCFS acquires the flexural rigidity of the plate is decreasing, as expected, the plate deflections are increasing.

4.3. Natural frequency analysis

Firstly, we consider an IF square Al/Al_2O_3 thin plate with the ratio $a/h = 100$. The fundamental frequency normalized by $\overline{\omega} = \omega\pi^2(a^2/h)\sqrt{\rho_m/E_m}$. The first five natural frequencies of the IF square with different boundary conditions and gradient index are given in Table 7. From the table results, it is observed that the present results are in favorable agreement with those reference solutions such as the exact method (Baferani, Saidi, and Jomehzadeh 2011), IGA-neu-CPT (Yin, Yu, and Liu 2013), MK-S-FSDT (Vu et al. 2017) and MK-N-RSHSDT (Vu, Curiel-Sosa, and Bui 2018b).

It is worth noting that by increasing the gradient indices, the magnitudes of natural frequency are decreasing. The plate boundary condition is a significant factor that affects its natural frequencies.

When the plate boundary condition changing from SFSF, SSSS, SCSC to CCCC leads to increasing the structural plate stiffnesses. As expected, the plate natural frequency magnitudes are increasing. The first six of mode shapes of the square plate with the boundary condition of the SCSC and using the gradient index $\eta = 1$ are illustrated in Figure 6.

Next, we investigate a clamped Al/Al_2O_3 IF circular plate using the different thickness-radius ratio of h/R. The normalized natural frequency $\tilde{\omega} = 100\omega h\sqrt{\rho_c/E_c}$ is calculated by the proposed RAESDT method and gathered in Table 8. It can be concluded the obtained results are close to

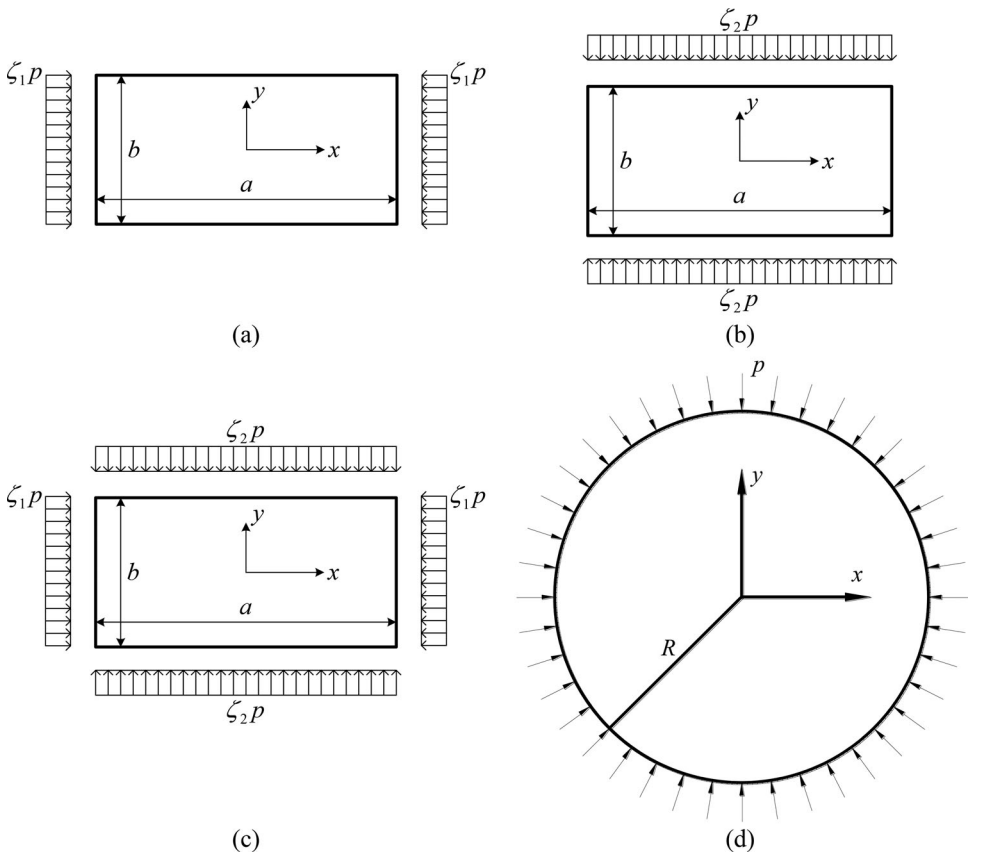

Figure 9. Compressive in-plane forces applied to plates: (a) along the x axis ($\zeta_1 = -1, \zeta_2 = 0$); (b) along the y axis ($\zeta_1 = 0, \zeta_2 = -1$); (c) biaxial axes ($\zeta_1 = -1, \zeta_2 = -1$); (d) radial direction.

the IGA-S-FSDT, IGA-FSDT (Yin et al. 2014) and IGA-HSDT (Tran, Ferreira, and Nguyen-Xuan 2013), Semi-analytical-FSDT (Hosseini-Hashemi, Fadaee, and Es'haghi 2010) and UM with FSDT (Ebrahimi, Rastgoo, and Atai 2009) solutions.

It is also worth pointing out that by increasing the thickness-radius ratios of the circular plate, the magnitudes of natural frequency are increasing. This is attributed to the increase in the plate thickness thereby increasing the overall stiffness of the plate. Figure 7 plots the first six mode shapes of the circular plate with clamped periphery and gradient index $\eta = 1$. We further investigate the influences of the boundary condition and gradient index on the fundamental frequency of the IF clamped circular plate. The first plate natural frequencies $\tilde{w}_1$ are presented in Table 9. As observed from this table, present results are in good agreement with the solutions obtained by IGA-FSDT and IGA-S-FSDT methods given by Yin et al. (2014). It should be noted that plate natural frequencies with clamped boundary are higher than those of both free and roller boundaries along the plate's periphery since the overall stiffness of the plate with clamped boundary is highest. However, increasing the gradient index value leads to reduction of magnitudes of the plate natural frequency due to lower the stiffness of the plate. Let us consider a sandwich FCHS $(1/8/1)$ square plate with the gradient index is fixed at $\eta = 1$ and two sides-thickness ratios $a/h = 10$ and 100. Its top and bottom faces are alumina and aluminum, respectively.

The normalized natural frequency $\tilde{\omega} = \omega(a^2/h)\sqrt{\rho_0/E_0}$ with $\rho_0 = 1.0$ and $E_0 = 1.0$ is computed by the present method for different types of plate boundary conditions of SSSS, CCCC and

Table 12. Comparison of the buckling load $\overline{N}_{cr}$ of IF rectangular plates Al/Al_2O_3 using the ratio $a/h = 100$.

		$a/b = 1.5$			$a/b = 1.0$		
		(ζ_1, ζ_2)			(ζ_1, ζ_2)		
η	Methods	−1,0	0,−1	−1,−1	−1,0	0,−1	−1,−1
(a) SFSF							
1	IGA-S-FSDT (Yin et al. 2014)	0.0714	0.1305	0.0702	0.1630	0.3497	0.1596
	Levy (Mohammadi, Saidi, and Jomehzadeh 2010)	0.0714	0.1305	0.0702	0.1630	0.3497	0.1712
	MK-R-STSDT(Vu et al. 2018a)	0.0716	0.1329	0.0705	0.1632	0.3535	0.1602
	MK-N-RSHSDT(Vu, Curiel-Sosa, and Bui 2018b)	0.0708	0.1268	0.0695	0.1619	0.3397	0.1582
	Present	0.0721	0.1315	0.0710	0.1641	0.3532	0.1608
2	IGA-S-FSDT (Yin et al. 2014)	0.0557	0.1018	0.0548	0.1272	0.2729	0.1245
	Levy (Mohammadi, Saidi, and Jomehzadeh 2010)	0.0557	0.1019	0.0548	0.1272	0.2729	0.1245
	MK-N-RSHSDT(Vu, Curiel-Sosa, and Bui 2018b)	0.0552	0.0989	0.0542	0.1264	0.2651	0.1235
	Present	0.0562	0.1034	0.0553	0.1288	0.2764	0.1262
(b) SSSS							
1	IGA-S-FSDT (Yin et al. 2014)	0.7429	0.3571	0.2472	0.6846	0.6846	0.3423
	Levy (Mohammadi, Saidi, and Jomehzadeh 2010)	0.7430	0.3572	0.2473	0.6848	0.6848	0.3424
	MK-R-STSDT (Vu et al. 2018a)	0.7478	0.3577	0.2477	0.6850	0.6850	0.3425
	MK-N-RSHSDT (Vu, Curiel-Sosa, and Bui 2018b)	0.7398	0.3412	0.2361	0.6695	0.6695	0.3347
	Present	0.7500	0.3587	0.2486	0.6840	0.6840	0.3420
2	IGA-S-FSDT (Yin et al. 2014)	0.5797	0.2787	0.1929	0.5342	0.5342	0.2671
	Levy (Mohammadi, Saidi, and Jomehzadeh 2010)	0.5798	0.2787	0.1930	0.5343	0.5343	0.2672
	MK-R-STSDT (Vu et al. 2018a)	0.5838	0.2791	0.1933	0.5346	0.5346	0.2673
	MK-N-RSHSDT (Vu, Curiel-Sosa, and Bui 2018b)	0.5325	0.2663	0.1843	0.5225	0.5225	0.2613
	Present	0.5995	0.2826	0.1957	0.5429	0.5429	0.2715
(c) SCSC							
1	IGA-S-FSDT (Yin et al. 2014)	1.2177	0.8622	0.6448	1.3161	1.1542	0.6554
	Levy (Mohammadi, Saidi, and Jomehzadeh 2010)	1.2181	0.8622	0.6450	1.3167	1.1544	0.6556
	MK-R-STSDT (Vu et al. 2018a)	1.2167	0.8649	0.6455	1.3224	1.1694	0.6579
	MK-N-RSHSDT (Vu, Curiel-Sosa, and Bui 2018b)	1.2200	0.8684	0.6467	1.3048	1.1538	0.6489
	Present	1.2239	0.8788	0.6517	1.3417	1.1850	0.6709
2	IGA-S-FSDT (Yin et al. 2014)	0.9502	0.6728	0.5031	1.0270	0.9006	0.5114
	Levy (Mohammadi, Saidi, and Jomehzadeh 2010)	0.9506	0.6728	0.5033	1.0274	0.9008	0.5116
	MK-R-STSDT (Vu et al. 2018a)	0.9511	0.6758	0.5045	1.0342	0.9145	0.5142
	MK-N-RSHSDT (Vu, Curiel-Sosa, and Bui 2018b)	0.9541	0.6783	0.5050	1.0200	0.9010	0.5070
	Present	0.9550	0.6850	0.5077	1.0352	0.9192	0.5217

tabulated in Table 10. It can be seen that the present results match excellently with Ritz-3D (Li, Iu, et al. 2008) solutions and are very close to the MK-N-RSHSDT (Vu, Curiel-Sosa, and Bui 2018b) solutions in cases of thin and thick plate. Furthermore, the increasing ratio a/h gains an increase with respect to the plate natural frequency because of increasing the material rigidity. As the plate boundary condition changes from CCCC to SSSS leading to the structure stiffness decrease, and the plate fundamental frequency decreases, as expected. Moreover, the thin plates are slightly more sensitive than the thick plate to material rigidity, this effect is a little lesser for CCCC plates as compared with SSSS plates. Figure 8 illustrates the first six mode shapes of the plate with fully clamped at all edges.

Another comparative verification of evaluating free vibration for sandwich Al/Al_2O_3 HCFS square plate with the SSSS boundary condition and the ratio $a/h = 10$ using different layer ratios and gradient indices is considered. Table 11 presents a comparison of the first mode of the plate, non-dimensional natural frequency $\bar{\omega}_1$ for six layer ratios and the gradient index $\eta = 0.5,\ 1,\ 5$ and 10 among the present approach and the other available methods such as the Ritz-3D (Li, Iu, et al. 2008), SSDT and TSDT (Zenkour 2005) and MK-N-RSHSDT (Vu, Curiel-Sosa, and Bui 2018b). Again, the obtained results are almost identical with those calculated by the Ritz-3D method.

It is also worth-mentioning that the frequencies increase with the decreasing amount of metal in the HCFS plate, and the effect of gradient index η on $1-0-1$ HCFS plate which is without

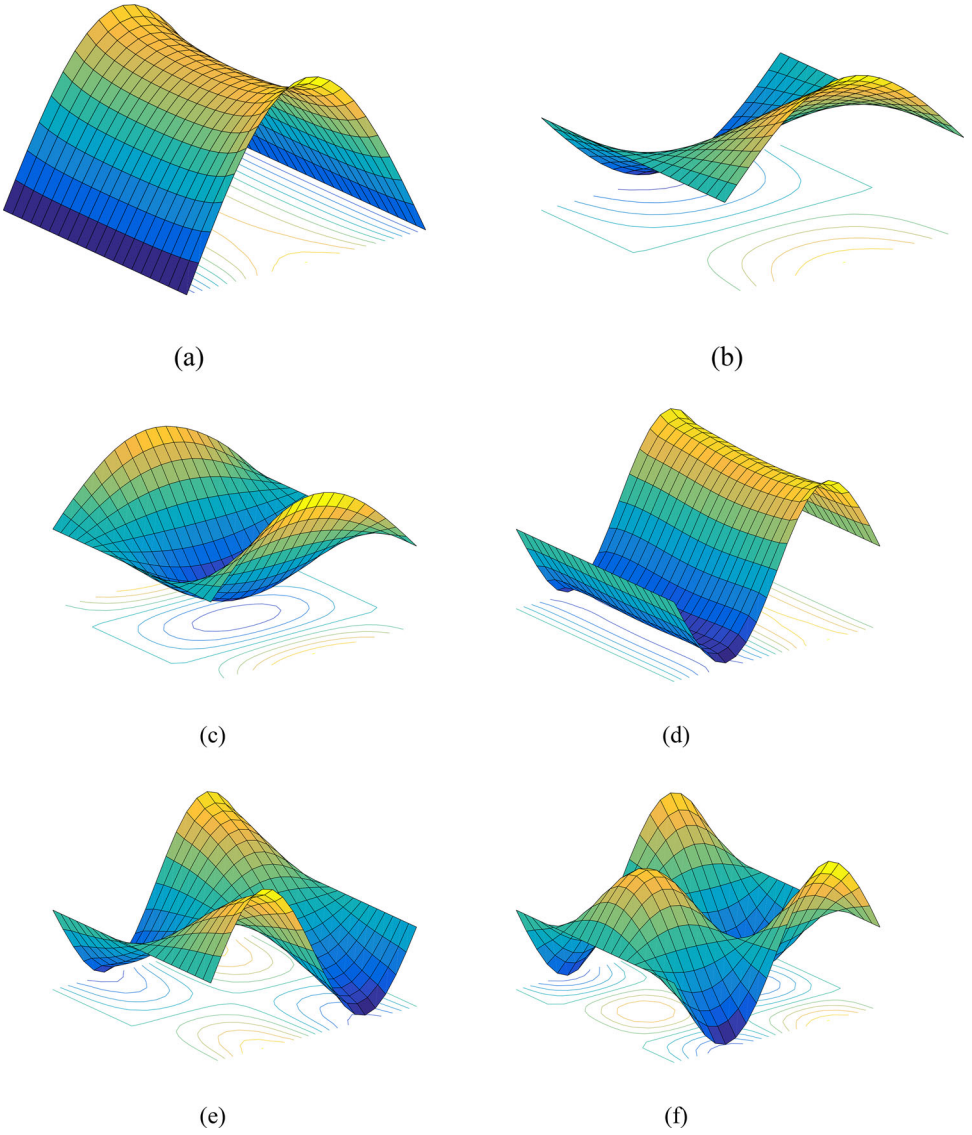

Figure 10. Buckling modes of the SFSFAl/Al_2O_3 IF rectangular plate with $\eta = 1$, $a/b = 0.5$, $a/h = 100$ and $(\zeta_1 = -1, \zeta_2 = 0)$: (a) Mode shape 1, (c) Mode shape 2, (d) Mode shape 3, (e) Mode shape 4, (f) Mode shape 5, (h) Mode shape 6.

the homogeneous core layer is greater than that of $1-2-1$ HCFS plate with homogeneous hardcore. Thus, it can be concluded that the developed RAESDT with meliorated MKI meshless method produce the results with good accuracies for the FG plate free vibration problems.

4.4. Buckling analysis

In this section, numerical examples in predicting the buckling loads of FG plates are presented and compared with results obtained by various methods available in the literature. The in-plane compression loads applied to the plate are depicted as Figure 9a–c for the rectangular plate. By imposing the equilibrium requirements, pre-buckling forces are expressed as follows:

Table 13. Comparison of the buckling load $\tilde{N}_{cr}$ of thick IF circular plateAl/ZrO_2^*.

h/R	Methods	$\eta = 0$	$\eta = 0.5$	$\eta = 2$	$\eta = 5$	$\eta = 10$
(a) Roller supported boundary						
0.10	TSDT (Ma and Wang 2004)	4.1502	5.7196	6.7780	7.4701	7.9733
	Unstrained TSDT (Saidi, Rasouli, and Sahraee 2009)	4.1503	5.7198	6.7783	7.4697	7.9730
	Present	4.2357	5.8986	6.9932	7.6589	8.1510
0.20	TSDT (Ma and Wang 2004)	4.0077	5.5213	6.5671	7.2408	7.7213
	Unstrained TSDT (Saidi, Rasouli, and Sahraee 2009)	4.0079	5.5217	6.5672	7.2407	7.7211
	Present	4.0914	5.6938	6.7757	7.4254	7.8944
0.25	TSDT (Ma and Wang 2004)	3.9072	5.3819	6.4176	7.0783	7.5424
	Unstrained TSDT (Saidi, Rasouli, and Sahraee 2009)	3.9072	5.3819	6.4179	7.0779	7.5425
	Present	3.9925	5.5534	6.6259	7.2642	7.7172
0.30	TSDT (Ma and Wang 2004)	3.7911	5.2206	6.2437	6.8893	7.3353
	Unstrained TSDT (Saidi, Rasouli, and Sahraee 2009)	3.7911	5.2208	6.2441	6.8892	7.3348
	Present	3.8812	5.3957	6.4567	7.0820	7.5169
(b) Clamped boundary						
0.10	TSDT (Ma and Wang 2004)	14.0890	19.4110	23.0740	25.4390	27.1330
	Unstrained TSDT (Saidi, Rasouli, and Sahraee 2009)	14.0890	19.4130	23.0750	25.4420	27.1310
	Present	14.4787	20.0042	23.7855	26.1792	27.8947
0.20	TSDT (Ma and Wang 2004)	12.5740	17.3110	20.8030	22.9710	24.4230
	Unstrained TSDT (Saidi, Rasouli, and Sahraee 2009)	12.5750	17.3100	20.8050	22.9690	24.4220
	Present	12.9268	17.8365	21.4519	23.6457	25.1096
0.25	TSDT (Ma and Wang 2004)	11.6380	16.0130	19.3770	21.4140	22.7250
	Unstrained TSDT (Saidi, Rasouli, and Sahraee 2009)	11.6390	16.0120	19.3780	21.4120	22.7250
	Present	11.9962	16.5395	20.0303	22.0973	23.4140
0.30	TSDT (Ma and Wang 2004)	10.6700	14.6720	17.8820	19.7800	20.9480
	Unstrained TSDT (Saidi, Rasouli, and Sahraee 2009)	10.6700	14.6720	17.8810	19.7780	20.9490
	Present	11.0591	15.2356	18.5808	20.5146	21.6868

$$\sigma_x^0 = \zeta_1 p \ , \ \sigma_y^0 = \zeta_2 p \ , \ \tau_{xy}^0 = 0 \qquad (38a, 38b, 38c)$$

where p denotes the in-plane loading; ζ_1, ζ_2 are state factors, i.e., these values are negative or positive determining that compression or tension states, respectively.

Firstly, a thin IF rectangular Al/Al_2O_3 plate having $a/h = 100$ with the different gradient indices, boundary conditions and ratios of aspect ratios a/b under the biaxial or uniform compressive loading. Table 12 presents the normalized buckling load $\overline{N}_{cr} = N_{cr}a^2/D_m$, where $D_m = E_m h^3/12(1-\upsilon^2)$ given by the present RAESDT and reference methods.

From the table results. It is clear that present results agree well with those obtained by the numerical method IGA using S-FSDT theory (Yin et al. 2014), and MK-based meshless method using R-STSDT (Vu et al. 2018a) and N-RSHSDT (Vu, Curiel-Sosa, and Bui 2018b) theories and the analytical solutions published in the literature (Mohammadi, Saidi, and Jomehzadeh 2010).

As the plate boundary types from SCSC, SSSS to SFSF, the structural stiffness of the plates is decreased, as a result, the buckling load values are decreased.

However, by decreasing gradient indices, the magnitudes of the buckling load are increasing. It is worth noting that the magnitudes of buckling load obtained from the biaxial compressive state are lower than those obtained from the uniform compressive loading state. The first six buckling mode shapes with the plate aspect ratio $a/b = 1.5$ and gradient index $\eta = 1$ under the uniform compression along the y-axis are shown in Figure 10.

Next, an Al/ZrO_2^* thick IF circular plate subjected to the radial compressive load p(see Figure 9d) is considered to validate the accuracy of the proposed theory with meliorated MKI based meshless method. Material properties of the circular plate are also calculated by the mixture rule given by Eq. (39). In Table 13, a comparison of the normalized critical buckling loads $\tilde{N}_{cr} = N_{cr}R^2p/D_m$ for the circular plate with the different gradient indices, thickness-to-radius ratios, and boundary conditions are realized, with the analytical methods of TSDT (Ma and Wang 2004) and unstrained TSDT (Saidi, Rasouli, and Sahraee 2009). From the results, it can be seen that the results of proposed RAESDT agree well with those obtained by the analytical methods for all

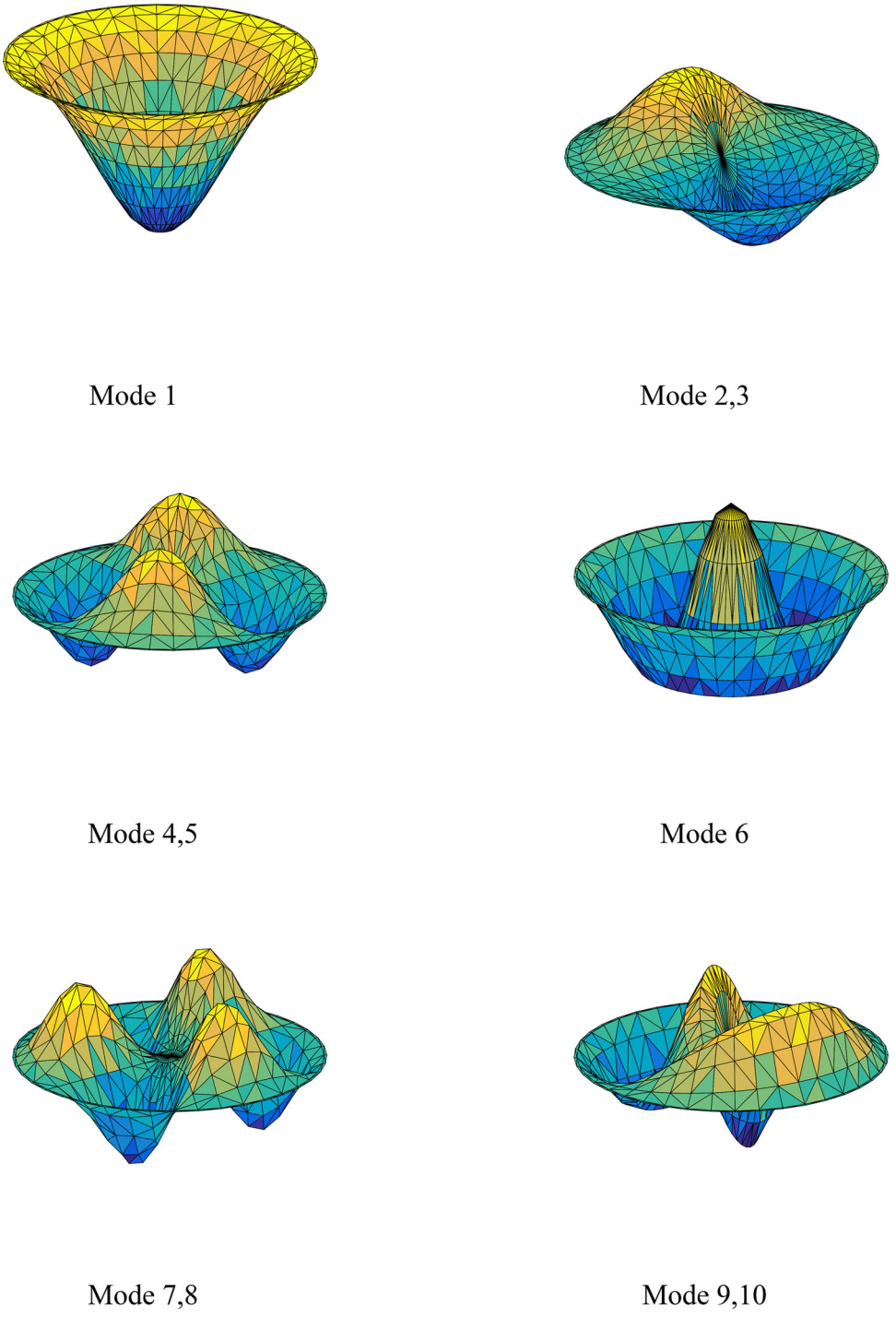

Figure 11. Buckling modes of clampedAl/ZrO_2^* IF circular plate ($\eta = 5,\ h/R = 0.1$).

gradient indices, thickness-to-radius ratios, and boundary conditions. It is relevant to conclude that increasing the thickness-to-radius ratio and decreasing gradient index η result in a reduction in the plate stiffness which is leading to decreasing buckling loads. The first ten buckling mode

Table 14. Comparison of the buckling load $\widehat{N}_{cr}$ of SSSS square plates HCFS Al/Al_2O_3 with $a/h = 10$ under uni-axial compression.

η	Methods	Layer ratios of plate HCFS (1/0/1)	(2/1/2)	(2/1/1)	(1/1/1)	(2/2/1)	(1/2/1)
0	SSDT (Zenkour 2005)	13.0061	13.0061	13.0061	13.0061	13.0061	13.0061
	TSDT (Reddy 2000)	13.0050	13.0050	13.0050	13.0050	13.0050	13.0050
	Quasi-3D-HSDT (Baferani, Saidi, and Jomehzadeh 2011)	12.9529	12.9529	12.9529	12.9529	12.9529	12.9529
	MK-N-RSHSDT (Vu, Curiel-Sosa, and Bui 2018b)	13.0031	13.0031	13.0031	13.0031	13.0031	13.0031
	Present	13.0923	13.0923	13.0923	13.0923	13.0923	13.0923
1	SSDT (Zenkour 2005)	5.1685	5.8412	6.1946	6.4654	6.9498	7.5063
	TSDT (Reddy 2000)	5.1671	5.8401	6.1939	6.4647	6.9494	7.5066
	Quasi-3D-HSDT (Baferani, Saidi, and Jomehzadeh 2011)	5.0614	5.7114	6.0547	6.3150	6.7841	7.3200
	MK-N-RSHSDT (Vu, Curiel-Sosa, and Bui 2018b)	5.1676	5.8401	6.1941	6.4640	6.9489	7.5043
	Present	5.2043	5.8810	6.2369	6.5083	6.9963	7.5544
5	SSDT (Zenkour 2005)	2.6601	3.0441	3.4045	3.5806	4.1129	4.7349
	TSDT (Reddy 2000)	2.6582	3.0426	3.4035	3.5796	4.1121	4.7347
	Quasi-3D-HSDT (Baferani, Saidi, and Jomehzadeh 2011)	2.6365	3.0079	3.3626	3.5301	4.0507	4.6470
	MK-N-RSHSDT (Vu, Curiel-Sosa, and Bui 2018b)	2.6600	3.0438	3.4055	3.5800	4.1136	4.7336
	Present	2.6805	3.0663	3.4302	3.6056	4.1429	4.7657
10	SSDT (Zenkour 2005)	2.4893	2.7484	3.1344	3.1946	3.1457	4.3818
	TSDT (Reddy 2000)	2.4873	2.7463	3.0919	3.1947	3.7075	4.2799
	Quasi-3D-HSDT (Baferani, Saidi, and Jomehzadeh 2011)	2.4722	2.7205	3.0607	3.1576	3.6617	4.2055
	MK-N-RSHSDT (Vu, Curiel-Sosa, and Bui 2018b)	2.4894	2.7479	3.0940	3.1955	3.7095	4.2793
	Present	2.5090	2.7687	3.1168	3.2187	3.7363	4.3086

Table 15. Comparison of the buckling load $\widehat{N}_{cr}$ of SSSS square plates HCFS Al/Al_2O_3 using $a/h = 10$ under bi-axial compression.

η	Methods	Layer ratios of plate HCFS (1/0/1)	(2/1/2)	(2/1/1)	(1/1/1)	(2/2/1)	(1/2/1)
0	SSDT (Zenkour 2005)	6.5030	6.5030	6.5030	6.5030	6.5030	6.5030
	TSDT (Reddy 2000)	6.5025	6.5025	6.5025	6.5025	6.5025	6.5025
	HSDT (Baferani, Saidi, and Jomehzadeh 2011)	6.4764	6.4764	6.4764	6.4764	6.4764	6.4764
	MK-N-RSHSDT(Vu, Curiel-Sosa, and Bui 2018b)	6.5022	6.5022	6.5022	6.5022	6.5022	6.5022
	Present	6.5470	6.5470	6.5470	6.5470	6.5470	6.5470
1	SSDT (Zenkour 2005)	2.5842	2.9206	3.0973	3.2327	3.4749	3.7531
	TSDT (Reddy 2000)	2.5836	2.9200	3.0970	3.2324	3.4747	3.7533
	HSDT (Baferani, Saidi, and Jomehzadeh 2011)	2.5307	2.8557	3.0273	3.1575	3.3920	3.6600
	MK-N-RSHSDT(Vu, Curiel-Sosa, and Bui 2018b)	2.5840	2.9203	3.0973	3.2322	3.4747	3.7524
	Present	2.6024	2.9407	3.1187	3.2545	3.4985	3.7776
5	SSDT (Zenkour 2005)	1.3300	1.5220	1.7022	1.7903	2.0564	2.3674
	TSDT (Reddy 2000)	1.3291	1.5213	1.7018	1.7898	2.0561	2.3673
	HSDT (Baferani, Saidi, and Jomehzadeh 2011)	1.3183	1.5040	1.6813	1.7650	2.0254	2.3235
	MK-N-RSHSDT(Vu, Curiel-Sosa, and Bui 2018b)	1.3301	1.5220	1.7028	1.7901	2.0569	2.3670
	Present	1.3403	1.5333	1.7152	1.8029	2.0716	2.3830
10	SSDT (Zenkour 2005)	1.2448	1.3742	1.5672	1.5973	1.5729	2.1909
	TSDT (Reddy 2000)	1.2436	1.3732	1.5460	1.5974	1.8538	2.1400
	HSDT (Baferani, Saidi, and Jomehzadeh 2011)	1.2361	1.3602	1.5303	1.5788	1.8308	2.1028
	MK-N-RSHSDT(Vu, Curiel-Sosa, and Bui 2018b)	1.2448	1.3740	1.5471	1.5979	1.8549	2.1398
	Present	1.2546	1.3844	1.5585	1.6095	1.8683	2.1544

shapes for the circle plate with $h/R = 0.1$ and $\eta = 5$ are shown in Figure 11. Last, an HCFS square plate with all edges SSSS and the ratio $a/h = 10$. Plate core is a pure ceramic, while top and bottom skins are metal-rich surfaces. Young modulus of the metal and ceramic constituents is expressed as $E_c = 380E_0$ and $E_m = 70E_0$ with $E_0 = 1$, respectively. The critical load is normalized by $\widehat{N}_{cr} = N_{cr}a^2/100E_0h^3$. For checking the present method accuracy, numerical solutions for different plate layer ratios and graded indices in the case of the uniaxial and biaxial compressive forces are compared with those generated by TSDT (Reddy 2000), quasi-3D-HSDT (Baferani, Saidi, and Jomehzadeh 2011), SSDT (Zenkour 2005), and MK-N-RSHSDT (Vu, Curiel-Sosa, and

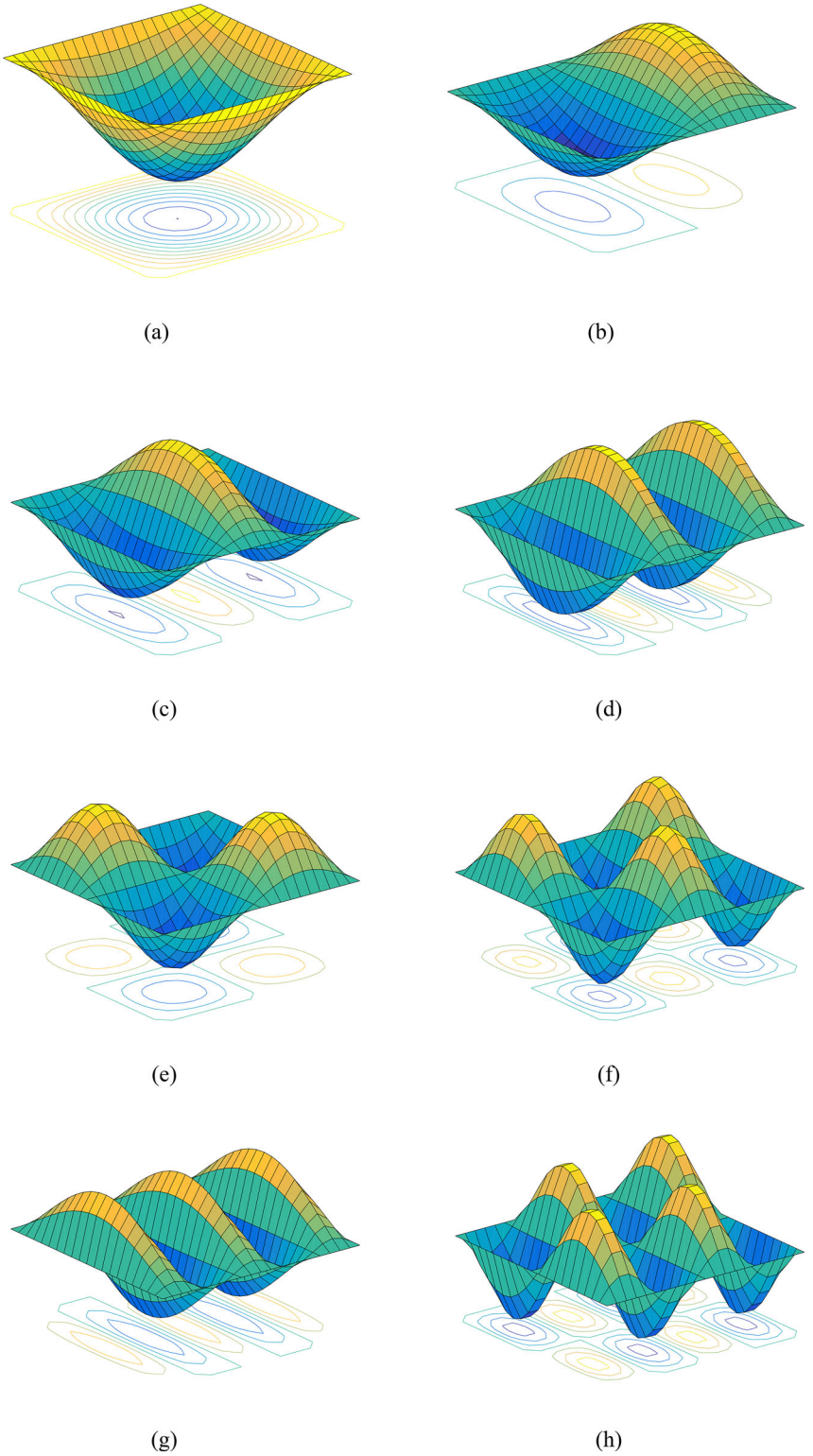

Figure 12. First eight buckling modes of the SSSSAl/Al_2O_3 square plate HCFS $(1/2/1)$ with $\eta = 5$, $a/h = 10$ and $(\zeta_1 = -1, \zeta_2 = 0)$: (a) Mode 1, (b) Mode 2, (c) Mode 3, (d) Mode 4, (e) Mode 5, (f) Mode 6, (g) Mode 7, (h) Mode 8.

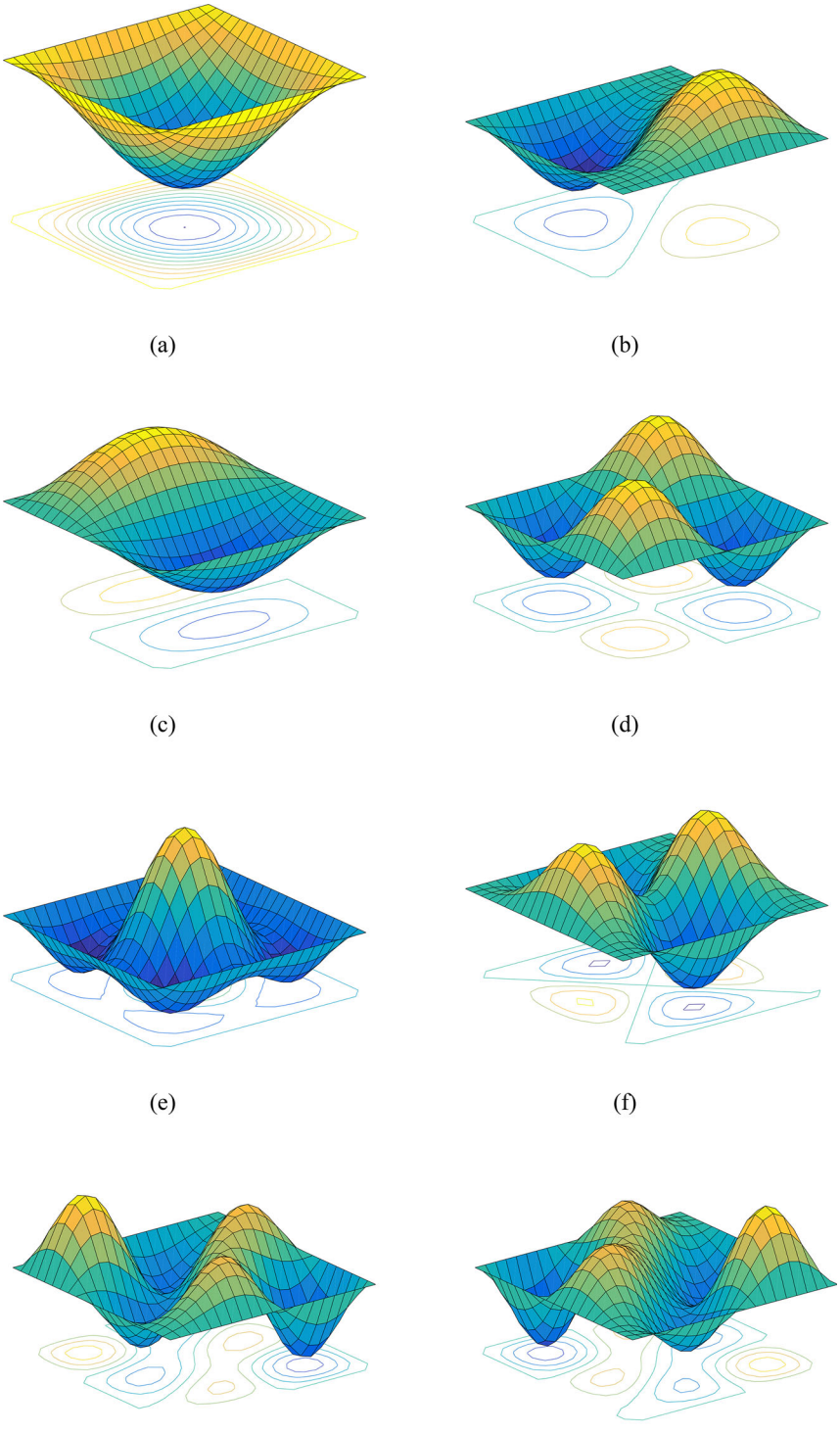

Figure 13. First eight buckling modes of the SSSSAl/Al_2O_3 square plate HCFS $(1/2/1)$ with $\eta = 5$, $a/h = 10$ and $(\zeta_1 = -1, \zeta_2 = -1)$: (a) Buckling mode 1, (b) Buckling mode 2, (c) Buckling mode 3, (d) Buckling mode 4, (e) Buckling mode 5, (f) Buckling mode 6, (g) Buckling mode 7, (h) Buckling mode 8.

Bui 2018b) and shown in Tables 14 and 15. A good agreement for all types of scheme of plates, graded indices and the case of compressive load is achieved. As seen from the tables that lowest critical load values are obtained in the case of homogeneous isotropic metal plate (last rows of Tables 14 and 15).

It is worth noting that the buckling load increases by the decrease of gradient index η, however, it decreases with decreasing the core-to-thickness ratio $(z_3 - z_2)/h$. It is shown that for both uni-axial and bi-axial compression, the buckling load decrease with the decrease of the material rigidity, which is due to the increase of gradient index η and the decrease of the core thickness for square plates HCFS. On the other hand, buckling loads in case of the biaxial compression are a half of those obtained in the case of uniform compression for the sandwich plate.

Figures 12 and 13 plot the first eight buckling modes for the plate with the layer thickness ratio $(1/2/1)$ and graded index $\eta = 5$ in case of the uniaxial and biaxial compression, respectively.

It can be concluded that the proposed RAESDT incorporating the MKI meshless with the new quadrature correlation function can predict very accurately the plate critical load with different plate geometries and layer ratios under different compression states.

5. Conclusions

A new four-unknown arctangent shear deformation theory integrated with meliorated moving kriging interpolation-based meshless method is developed for bending, free vibration and compressive buckling analyses of sandwich FG plates. The present approach describes the shear stress distribution model across the plate thickness respecting the zero traction boundary conditions on the top and bottom surfaces without using the external shear correction factor by an arctangent-exponential function which is the combination of the elementary functions having many odd powers in its series expansion, hence the proposed function is richer than third-order functions getting the better representation of the transverse shear stress used in the plate analysis. By separating the transverse deflection into bending and shear parts, the present theory has only four unknowns as against five or more unknowns in the traditional HSDT, therefore, it reduces substantially the computational cost. A new quadrature correlation function is also proposed to stabilize numerical solutions of the traditional moving kriging interpolation-based meshless approach obtaining accurate solutions. The accuracy of this method is ascertained by comparing the obtained solutions with those generated by available methods, and excellent agreement was observed for all study cases. The proposed formulations in this paper are general and it could be applied for the plate analysis with complicated geometries and arbitrary boundary conditions.

It is expected that the present plate theory could be applied to FG plates and shells for both geometric linear and nonlinear analyses using both numerical and analytical methods. Furthermore, the proposed arctangent distributed function can be combined with quasi-3D theories with considering stretching and shear deformation effects to get a better computational efficiency.

Acknowledgments

The authors would like to thank the three anonymous reviewers for their insightful suggestions and careful reading of the manuscript. This research was supported by the Vietnam National Foundation for Science and Technology Development (NAFOSTED) under grant number 107.01-2018.319.

Conflict of interest

The authors declare that there is no conflict of interest.

Funding

This research is funded by Vietnam National Foundation for Science and Technology Development (NAFOSTED) under grant number 107.01-2018.319.

References

Amirpour, M., S. Bickerton, E. Calius, R. Das, and B. Mace. 2019. Numerical and experimental study on deformation of 3D-printed polymeric functionally graded plates: 3D-digital image correlation approach. *Composite Structures* 211:481–9. doi:10.1016/j.compstruct.2019.01.014.

Amirpour, M., S. Bickerton, E. Calius, B. Mace, and R. Das. 2018. Numerical and experimental study on free vibration of 3D-printed polymeric functionally graded plates. *Composite Structures* 189:192–205. doi:10.1016/j.compstruct.2018.01.056.

Baferani, A. H., A. R. Saidi, and E. Jomehzadeh. 2011. An exact solution for free vibration of thin functionally graded rectangular plates. *Proceedings of the Institution of Mechanical Engineers, Part C: Journal of Mechanical Engineering Science* 225 (3):526–3. doi:10.1243/09544062JMES2171.

Bessaim, A., M. S. A. Houari, A. Tounsi, S. R. Mahmoud, and E. A. Adda Bedia. 2013. A new higher-order shear and normal deformation theory for the static and free vibration analysis of sandwich plates with functionally graded isotropic face sheets. *Journal of Sandwich Structures and Materials* 15 (6):671–703. doi:10.1177/1099636213498888.

Bui, Q. T., N. T. Nguyen, and D. H. Nguyen. 2009. A moving kriging interpolation-based meshless method for numerical simulation of Kirchhoff plate problems. *International Journal for Numerical Methods in Engineering* 77 (10):1371–95. doi:10.1002/nme.2462.

Carrera, E., S. Brischetto, M. Cinefra, and M. Soave. 2011. Effects of thickness stretching in functionally graded plates and shells. *Composites Part B: Engineering* 42 (2):123–33. doi:10.1016/j.compositesb.2010.10.005.

Cheshmeh, E., M. Karbon, A. Eyvazian, D. W. Jung, M. Habibi, and M. Safarpour. 2020. Buckling and vibration analysis of FG-CNTRC plate subjected to thermo-mechanical load based on higher order shear deformation theory. *Mechanics Based Design of Structures and Machines*. doi:10.1080/15397734.2020.1744005.

Chu, F., J. He, L. Wang, and Z. Zhong. 2016. Buckling analysis of functionally graded thin plate with in-plane material inhomogeneity. *Engineering Analysis with Boundary Elements* 65:112–25. doi:10.1016/j.enganabound.2016.01.007.

Dastjerdi, R. M., S. Rashahmadi, and S. A. Meguid. 2020. Electro-mechanical performance of smart piezoelectric nanocomposite plates reinforced by zinc oxide and gallium nitride nanowires. *Mechanics Based Design of Structures and Machines*. doi:10.1080/15397734.2020.1766496.

Ebrahimi, F., A. Rastgoo, and A. A. Atai. 2009. A theoretical analysis of smart moderately thick shear deformable annular functionally graded plate. *European Journal of Mechanics: A/Solids* 28 (5):962–73. doi:10.1016/j.euromechsol.2008.12.008.

Farzad, E., M. Nouraei, and A. Dabbagh. 2020. Modeling vibration behavior of embedded graphene-oxide powder-reinforced nanocomposite plates in thermal environment. *Mechanics Based Design of Structures and Machines* 48 (2):217–40. doi:10.1080/15397734.2019.1660185.

Garg, A., H. D. Chalak, and A. Chakrabarti. 2020. Bending analysis of functionally graded sandwich plates using HOZT including transverse displacement effects. *Mechanics Based Design of Structures and Machines*. doi:10.1080/15397734.2020.1814157.

Hachemi, M., and S. M. H. Cherif. 2020. Free vibration of composite laminated plate with complicated cutout. *Mechanics Based Design of Structures and Machines* 48 (2):192–216. doi:10.1080/15397734.2019.1633341.

Hosseini-Hashemi, S., M. Fadaee, and M. Es'haghi. 2010. A novel approach for in-plane/out-of-plane frequency analysis of functionally graded circular/annular plates. *International Journal of Mechanical Sciences* 52 (8):1025–35. doi:10.1016/j.ijmecsci.2010.04.009.

Karama, M., K. S. Afaq, and S. Mistou. 2003. Mechanical behaviour of laminated composite beam by the new multi-layered laminated composite structures model with transverse shear stress continuity. *International Journal of Solids and Structures* 40 (6):1525–46. doi:10.1016/S0020-7683(02)00647-9.

Kiendl, J., Y. Bazilevs, M. C. Hsu, R. Wuchner, and K. U. Bletzinger. 2010. The bending strip method for isogeometric analysis of Kirchhoff–Love shell structures comprised of multiple patches. *Computer Methods in Applied Mechanics and Engineering* 199 (37–40):2403–16. doi:10.1016/j.cma.2010.03.029.

Kirchhoff, G. 1850. Über das gleichgewicht und die bewegung einer elastischen scheibe [On the balance and the movement of a resilient disc. *Journal Für Die Reine Und Angewandte Mathematik* 40:51–88. doi:10.1515/crll.1850.40.5.

Lee, Y. Y., X. Zhao, and K. M. Liew. 2009. Thermoelastic analysis of functionally graded plates using the element-free kp-Ritz method. *Smart Materials and Structures* 18 (3):035007. doi:10.1088/0964-1726/18/3/035007.

Li, Q., V. P. Iu, and K. P. Kou. 2008. Three-dimensional vibration analysis of functionally graded material sandwich plates. *Journal of Sound and Vibration* 311 (1–2):498–515. doi:10.1016/j.jsv.2007.09.018.

Li, X. Y., H. J. Ding, and W. Q. Chen. 2008. Elasticity solutions for a transversely isotropic functionally graded circular plate subject to an axisymmetric transverse load QRK. *International Journal of Solids and Structures* 45 (1):191–210. doi:10.1016/j.ijsolstr.2007.07.023.

Lieu, Q. X., S. Lee, J. Kang, and J. Lee. 2018. Bending and free vibration analyses of in-plane bi-directional functionally graded plates with variable thickness using isogeometric analysis. *Composite Structures* 192:434–51. doi:10.1016/j.compstruct.2018.03.021.

Liew, K. M., X. Zhao, and A. J. M. Ferreira. 2011. A review of meshless methods for laminated and functionally graded plates and shells. *Composite Structures* 93 (8):2031–41. doi:10.1016/j.compstruct.2011.02.018.

Lim, T.-C. 2016. Higher-order shear deformation of very thick simply supported equilateral triangular plates under uniform load. *Mechanics Based Design of Structures and Machines* 44 (4):514–22. doi:10.1080/15397734.2015.1124784.

Liu, D. Y., C. Y. Wang, and W. Q. Chen. 2010. Free vibration of FGM plates with in-plane material inhomogeneity. *Composite Structures* 92 (5):1047–51. doi:10.1016/j.compstruct.2009.10.001.

Love, A. E. H. 1888. The small free vibrations and deformation of a thin elastic shell. *Philosophical Transactions of the Royal Society A: Mathematical, Physical and Engineering Sciences* 179:491–546. doi:10.1098/rsta.1888.0016.

Ma, L. S., and T. J. Wang. 2004. Relationship between axisymmetric bending and buckling solutions of FGM circular plates based on third-order plate theory and classical plate theory. *International Journal of Solids and Structures* 41 (1):85–101. doi:10.1016/j.ijsolstr.2003.09.008.

Menasria, A., A. Kaci, and A. A. Bousahla. 2020. A four-unknown refined plate theory for dynamic analysis of FG-sandwich plates under various boundary conditions. *Steel and Composite Structures* 36 (3):355–67. doi:10.12989/scs.2020.36.3.355.

Mindlin, R. D. 1951. Influence of rotatory inertia and shear on flexural motions of isotropic, elastic plates. *Journal of Applied Mechanics* 18:31–8.

Mohammadi, M., A. Saidi, and E. Jomehzadeh. 2010. Levy solution for buckling analysis of functionally graded rectangular plates. *Applied Composite Materials* 17 (2):81–93. doi:10.1007/s10443-009-9100-z.

Neves, A. M. A., A. J. M. Ferreira, E. Carrera, M. Cinefra, R. M. N. Jorge, and C. M. M. Soares. 2012. Static analysis of functionally graded sandwich plates according to a hyperbolic theory considering zig-zag and warping effects. *Advances in Engineering Software* 52:30–43. doi:10.1016/j.advengsoft.2012.05.005.

Neves, A. M. A., A. J. M. Ferreira, E. Carrera, M. Cinefra, C. M. C. Roque, R. M. N. Jorge, and C. M. M. Soares. 2013. Static free vibration and buckling analysis of isotropic and sandwich functionally graded plates using a quasi-3D higher-order shear deformation theory and a meshless technique. *Composites Part B: Engineering* 44 (1):657–74. doi:10.1016/j.compositesb.2012.01.089.

Rahmani, M. C., A. Kaci, A. A. Bousahla, F. Bourada, A. Tounsi, and E. A. A. Bedia. 2020. Influence of boundary conditions on the bending and free vibration behavior of FGM sandwich plates using a four-unknown refined integral plate theory. *Computers and Concrete* 25 (3):225–44. doi:10.12989/CAC.2020.25.3.225.

Reddy, J. N. 1984. A simple higher-order theory for laminated composite plates. *Journal of Applied Mechanics* 51 (4):745–52. doi:10.1115/1.3167719.

Reddy, J. N., C. M. Wang, and S. Kitipornchai. 1999. Axisymmetric bending of functionally graded circular and annular plates. *European Journal of Mechanics: A/Solids* 18 (2):185–99. doi:10.1016/S0997-7538(99)80011-4.

Reddy, J. N. 2000. Analysis of functionally graded plates. *International Journal for Numerical Methods in Engineering* 47 (1–3):663–84. doi:10.1002/(SICI)1097-0207(20000110/30)47:1/3 < 663::AID-NME787 > 3.0.CO;2-8.

Reissner, E. 1945. The effect of transverse shear deformation on the bending of elastic plates. *Journal of Applied Mechanics* 12:69–7.

Saidi, A. R., A. Rasouli, and S. Sahraee. 2009. Axisymmetric bending and buckling analysis of thick functionally graded circular plates using unconstrained third-order shear deformation plate theory. *Composite Structures* 89 (1):110–9. doi:10.1016/j.compstruct.2008.07.003.

Senthilnathan, N. R., S. P. Lim, K. H. Lee, and S. T. Chow. 1987. Buckling of shear-deformable plates. *Journals: The American Institute of Aeronautics and Astronautics: AIAA* 25 (9):1268–71. doi:10.2514/3.48742.
Soldatos, K. P. 1992. A transverse shear deformation theory for homogeneous monoclinic plates. *Acta Mechanica* 94 (3–4):195–220. doi:10.1007/BF01176650.
Shi, G. 2007. A new simple third-order shear deformation theory of plates. *International Journal of Solids and Structures* 44 (13):4399–417. doi:10.1016/j.ijsolstr.2006.11.03.
Timoshenko, S. P., and S. Woinowsky-Kriger. 1959. *Theory of plates and shells*. New York: McGraw-Hill.
Thai, C. H., N. V. D. Vuong, and H. Nguyen-Xuan. 2016. An improved moving kriging-based meshfree method for static, dynamic and buckling analyses of functionally graded isotropic and sandwich plates. *Engineering Analysis with Boundary Elements* 64:122–36. doi:10.1016/j.enganabound.2015.12.003.
Touratier, M. 1991. An efficient standard plate theory. *International Journal of Engineering Science* 29 (8):901–16. doi:10.1016/0020-7225(91)90165-Y.
Tran, L. V., A. J. M. Ferreira, and H. Nguyen-Xuan. 2013. Isogeometric analysis of functionally graded plates using higher-order shear deformation theory. *Composites Part B: Engineering* 51:368–83. doi:10.1016/j.compositesb.2013.02.045.
Vu, T. V., J. L. Curiel-Sosa, and T. Q. Bui. 2018b. A refined sin hyperbolic shear deformation theory for sandwich FG plates by enhanced meshfree with new correlation function. *International Journal of Mechanics and Materials in Design* 15 (3):647–69. doi:10.1007/s10999-018-9430-9.
Vu, T. V., A. Khosravifard, M. R. Hematiyan, and T. Q. Bui. 2018a. A new refined simple TSDT-based effective meshfree method for analysis of through-thickness FG plates. *Applied Mathematical Modelling* 57:514–34. doi:10.1016/j.apm.2018.01.004.
Vu, T. V., A. Khosravifard, M. R. Hematiyan, and T. Q. Bui. 2018c. Enhanced meshfree method with new correlation functions for functionally graded plates using a refined inverse sin shear deformation plate theory. *European Journal of Mechanics: A/Solids* 74:160–75. doi:10.1016/j.euromechsol.2018.11.005.
Vu, T.-V., N.-H. Nguyen, A. Khosravifard, M. R. Hematiyan, S. Tanaka, and T. Q. Bui. 2017. A simple FSDT-based meshfree method for analysis of functionally graded plates. *Engineering Analysis with Boundary Elements* 79:1–12. doi:10.1016/j.enganabound.2017.03.002.
Vu, T. V., and V. S. Phan. 2017. A modified moving kriging interpolation-based meshfree method with refined sinusoidal shear deformation theory for analysis of functionally graded plates. In *ACOME 2017: Proceedings of the International Conference on Advances in Computational Mechanics 2017*, ed. H. Nguyen-Xuan, P. Phung-Van, and T. Rabczuk, 485–501. Singapore: Springer. doi:10.1007/978-981-10-7149-2_33.
Yin, S. H., T. T. Yu, and P. Liu. 2013. Free vibration analyses of FGM thin plates by isogeometric analysis based on classical plate theory and physical neutral surface. *Advances in Mechanical Engineering* 5. doi:10.1155/2013/:634584.
Yin, S., J. S. Hale, T. Yu, T. Q. Bui, and S. P. A. Bordas. 2014. Isogeometric locking-free plate element: A simple first order shear deformation theory for functionally graded plates. *Composite Structures* 118:121–38. doi:10.1016/j.compstruct.2014.07.028.
Zenkour, A. M. A. 2005. A comprehensive analysis of functionally graded sandwich plates: Part 2: Buckling and free vibration. *International Journal of Solids and Structures* 42 (18–19):5243–58. doi:10.1016/j.ijsolstr.2005.02.016.

Appendix A

The coefficients appeared in Eq. (23b) are as follows:

$$\tilde{A}_{11} = \int_{-h/2}^{h/2} \tilde{Q}_{11} dz,\ \tilde{A}_{12} = \int_{-h/2}^{h/2} \tilde{Q}_{12} dz,\ \tilde{A}_{13} = 0,\ \tilde{A}_{21} = \int_{-h/2}^{h/2} \tilde{Q}_{21} dz,\ \tilde{A}_{22} = \int_{-h/2}^{h/2} \tilde{Q}_{22} dz,\ \tilde{A}_{23} = 0,\ \tilde{A}_{31} = 0,$$

$$\tilde{A}_{32} = 0,\ \tilde{A}_{33} = \int_{-h/2}^{h/2} \tilde{Q}_{33} dz.$$

$$\tilde{B}_{11} = \int_{-h/2}^{h/2} z\tilde{Q}_{11} dz,\ \tilde{B}_{12} = \int_{-h/2}^{h/2} z\tilde{Q}_{12} dz,\ \tilde{B}_{13} = 0,\ \tilde{B}_{21} = \int_{-h/2}^{h/2} z\tilde{Q}_{21} dz,\ \tilde{B}_{22} = \int_{-h/2}^{h/2} z\tilde{Q}_{22} dz,\ \tilde{B}_{23} = 0,$$

$$\tilde{B}_{31} = 0,\ \tilde{B}_{32} = 0,\ \tilde{B}_{33} = \int_{-h/2}^{h/2} z\tilde{Q}_{33} dz.$$

$$\tilde{C}_{11}=\int_{-h/2}^{h/2} z^2\tilde{Q}_{11}dz,\ \tilde{C}_{12}=\int_{-h/2}^{h/2} z^2\tilde{Q}_{12}dz,\ \tilde{C}_{13}=0,\ \tilde{C}_{21}=\int_{-h/2}^{h/2} z^2\tilde{Q}_{21}dz,\ \tilde{C}_{22}=\int_{-h/2}^{h/2} z^2\tilde{Q}_{22}dz,\ \tilde{C}_{23}=0,$$

$$\tilde{C}_{31}=0,\ \tilde{C}_{32}=0,\ \tilde{C}_{33}=\int_{-h/2}^{h/2} z^2\tilde{Q}_{33}dz$$

$$\tilde{E}_{11}=\int_{-h/2}^{h/2} g(z)\tilde{Q}_{11}dz,\ \tilde{E}_{12}=\int_{-h/2}^{h/2} g(z)\tilde{Q}_{12}dz,\ \tilde{E}_{13}=0,\ \tilde{E}_{21}=\int_{-h/2}^{h/2} g(z)\tilde{Q}_{21}dz,\ \tilde{E}_{22}=\int_{-h/2}^{h/2} g(z)\tilde{Q}_{22}dz,\ \tilde{E}_{23}=0,$$

$$\tilde{E}_{31}=0,\ \tilde{E}_{32}=0,\ \tilde{E}_{33}=\int_{-h/2}^{h/2} g(z)\tilde{Q}_{33}dz$$

$$\tilde{K}^{\varepsilon}_{11}=\int_{-h/2}^{h/2} zg(z)\tilde{Q}_{11}dz,\ \tilde{K}^{\varepsilon}_{12}=\int_{-h/2}^{h/2} zg(z)\tilde{Q}_{12}dz,\ \tilde{K}^{\varepsilon}_{13}=0,\ \tilde{K}^{\varepsilon}_{21}=\int_{-h/2}^{h/2} zg(z)\tilde{Q}_{21}dz,\ \tilde{K}^{\varepsilon}_{22}=\int_{-h/2}^{h/2} zg(z)\tilde{Q}_{22}dz,$$

$$\tilde{K}^{\varepsilon}_{23}=0,\ \tilde{K}^{\varepsilon}_{31}=\int_{-h/2}^{h/2} zg(z)\tilde{Q}_{31}dz,\ \tilde{K}^{\varepsilon}_{32}=0,\ \tilde{K}^{\varepsilon}_{33}=\int_{-h/2}^{h/2} zg(z)\tilde{Q}_{33}dz$$

$$\tilde{H}_{11}=\int_{-h/2}^{h/2} g^2(z)\tilde{Q}_{11}dz,\ \tilde{H}_{12}=\int_{-h/2}^{h/2} g^2(z)\tilde{Q}_{12}dz,\ \tilde{H}_{13}=0,\ \tilde{H}_{21}=\int_{-h/2}^{h/2} g^2(z)\tilde{Q}_{21}dz,\ \tilde{H}_{22}=\int_{-h/2}^{h/2} g^2(z)\tilde{Q}_{22}dz,$$

$$\tilde{H}_{23}=0,\ \tilde{H}_{31}=\int_{-h/2}^{h/2} g^2(z)\tilde{Q}_{31}dz,\ \tilde{H}_{32}=0,\ \tilde{H}_{33}=\int_{-h/2}^{h/2} g^2(z)\tilde{Q}_{33}dz$$

$$\tilde{D}^{s}_{11}=\int_{-h/2}^{h/2}\left[\frac{\partial f(z)}{\partial z}\right]^2\tilde{G}_{11}dz,\ \tilde{D}^{s}_{12}=0,\ \tilde{D}^{s}_{21}=0,\ \tilde{D}^{s}_{22}=\int_{-h/2}^{h/2}\left[\frac{\partial f(z)}{\partial z}\right]^2\tilde{G}_{22}dz$$

the coefficients $\tilde{Q}_{ij},\tilde{G}_{ij}$ can be calculated by

$$\tilde{Q}_{11}=\tilde{Q}_{22}=\frac{E(z)}{1-\nu^2(z)},\ \tilde{Q}_{12}=\tilde{Q}_{21}=\frac{\nu(z)E(z)}{1-\nu^2(z)},\ \tilde{Q}_{13}=\tilde{Q}_{31}=\tilde{Q}_{23}=\tilde{Q}_{32}=0,\ \tilde{Q}_{33}=\frac{[1-\nu(z)]E(z)}{2[1-\nu^2(z)]},$$

$$\tilde{G}_{11}=\tilde{G}_{22}=\frac{E(z)}{2[1+\nu(z)]},\ \tilde{G}_{12}=\tilde{G}_{21}=0$$

Appendix B

The mass matrix $\mathbf{m}=\begin{bmatrix}\tilde{I}_0 & \tilde{I}_1 & \tilde{I}_3\\ \tilde{I}_1 & \tilde{I}_2 & \tilde{I}_4\\ \tilde{I}_3 & \tilde{I}_4 & \tilde{I}_5\end{bmatrix}$ with coefficients are as follows:

$$\tilde{I}_0=\int_{-h/2}^{h/2}\rho(z)dz,\ \tilde{I}_1=\int_{-h/2}^{h/2} z\rho(z)dz,\ \tilde{I}_2=\int_{-h/2}^{h/2} z^2\rho(z)dz,\ \tilde{I}_3=\int_{-h/2}^{h/2} g\rho(z)dz,\ \tilde{I}_4=\int_{-h/2}^{h/2} zg\rho(z)dz,\ \tilde{I}_5=\int_{-h/2}^{h/2} g^2\rho(z)dz$$